Optimal Orbit Altitude of Satellite Formations for Across-Track SAR Interferometry

Francesca Scala and Michelangelo Villano, *Senior Member, IEEE*

***Abstract*—Interferometric synthetic aperture radar (InSAR) is a well-known technique for a wide range of remote sensing applications, among which is the generation of accurate, high-resolution digital elevation models (DEMs). The selection of the orbit altitude for InSAR systems is currently based on the heritage of previous SAR missions, for which altitudes lower than 500 km are typically avoided. This article presents a novel criterion for optimizing the orbit altitude for InSAR missions when considering a formation of two or more satellites. Such a criterion is based on the minimization of the total energy required by the instrument and the control system while ensuring DEM accuracy and posting over a given observed area. This work considers both the well-known helix formation and an innovative fixed-baseline configuration and showcases specific design examples that combine the potential of both options. The analyses show that orbit altitudes around 400 km, i.e., lower than those that are typically considered nowadays, lead to a reduction of energy consumption, especially as the orbit duty cycle increases. The increased energy demand of the control, in fact, is compensated by the decreased energy demand of the radar. In addition, when a satellite formation operates with short fixed baselines once per month, the increase in energy demand per orbit of a traditional helix configuration has a minimal impact on the system design while providing notable observation advantages. The outcomes of these analyses are of paramount relevance for the design of optimized future InSAR missions for DEM generation.**

***Index Terms*—Across-track synthetic aperture radar (SAR) interferometry, closed loop control, digital elevation model (DEM), Earth observing system, formation flying, low Earth orbit (LEO), relative motion.**

I. Introduction

In THE last decades, interferometric synthetic aperture radar (InSAR) has gained increasing importance in the field of remote sensing in low Earth orbit (LEO). Most studies are driven by the need for more accurate information on numerous geophysical parameters in nearly all-weather day and night conditions [1], [2], [3], [4]. The power of InSAR lies in the possibility of coherently combining two or more complex synthetic aperture radar (SAR) images characterized by a temporal or a spatial baseline [1]. In this context, across-track interferometric SAR (XTI-SAR) has seen significant advancement in producing high-resolution digital elevation models (DEMs) [5], [6], [7]. Single-pass XTI-SAR removes temporal decorrelation, which impacts the repeat pass approach of monolithic architectures [6], [8], and requires two antennas separated in the across-track direction. This layout can be acquired with two different approaches: a single platform with two instruments, one of which could be mounted at the edges of a boom [9], [10], or multiple instruments mounted on multiple satellites. One of the first experiments in this field was the TOPSAR radar system with airborne C-band SAR. The system featured two antennas mounted on a single platform with a cross-track separation of about 2.5 m. This setup showed promising results in improving the performance of the SAR system, and it was subsequently applied to space missions [9]. Following this experiment, the Shuttle Radar Topography Mission (SRTM) was operated for ten days by the Space Shuttle Endeavour. It marked a significant advancement in acquiring 3-D images of the Earth's surface [11]. The SRTM was the first experiment to demonstrate the benefit of spaceborne single-pass InSAR for near-global high-resolution DEMs, thanks to a 60-m mast that extends from the Shuttle payload area [11]. However, the use of a deployable boom for single-pass InSAR, as in the SRTM experiment, poses severe limitations on the maximum baseline that can be achieved, which in most cases only represents a very small fraction of the optimum one, impacting the height accuracy of the DEM. Furthermore, once the boom is deployed, its length cannot be modified or adjusted during the mission, preventing the possibility of dynamically optimizing or correcting the baseline for various mission requirements or interferometric applications. In addition, it poses a risk to the overall mission in case of a failure or malfunction during the deployment. At the same time, vibrations or misalignments in the boom directly impact the stability of the baseline and, consequently, the interferometric phase accuracy of the radar signal, leading to reduced accuracy of the DEMs.

To overcome such limitations, formation flying of satellites for InSAR has been investigated, leading to the TanDEM-X mission. Launched in 2010, TanDEM-X has become one of the most important bistatic missions employing a two-satellite formation for single-pass InSAR [12], [13]. Thanks to the formation geometry based on the helix configuration [13], [14], [15], TanDEM-X was able to provide unprecedented

Received 11 May 2025; revised 9 October 2025 and 12 January 2026; accepted 12 January 2026. Date of publication 20 January 2026; date of current version 2 February 2026. Co-funded by the European Union (ERC, DRITUCS, 101076275). Views and opinions expressed are however those of the authors only and do not necessarily reflect those of the European Union or the European Research Council Executive Agency. Neither the European Union nor the granting authority can be held responsible for them. *(Corresponding author: Francesca Scala.)*

Francesca Scala is with the Microwaves and Radar Institute, German Aerospace Center (DLR), 82234 Weßling, Germany, and also with Starion Group, European Space Agency (ESA)-ESTEC, 2201 AZ Noordwijk, The Netherlands (e-mail: francesca1.scala@polimi.it).

Michelangelo Villano is with the Microwaves and Radar Institute, DLR, 82234 Weßling, Germany (e-mail: Michelangelo.Villano@dlr.de).

Digital Object Identifier 10.1109/TGRS.2026.3656250

accuracy and resolution of the DEM on a global scale. The requirements of 12-m horizontal resolution and 2-m relative vertical accuracy (to be intended as 90th- percentile) for terrain slopes less than 20%, in fact, were not only met, but even exceeded [16]. The helix configuration consists of a secondary spacecraft moving around the primary satellite on a closed trajectory, with helical behavior. This design was selected to obtain a baseline that slowly varies in the hundreds of meters range for the data acquisition of the X-band SAR instruments [14], [17]. Another relevant study on single-pass InSAR is based on the MirrorSAR multibaseline concept, where three small receive-only satellites were conceived as add-ons for the high-resolution wide-swath (HRWS) X-band mission [18]. This concept is based on the possibility of employing multiple nested helix trajectories around the primary satellite to acquire multiple baselines in a single pass. A SAR system, where the backscattered radar signal is simultaneously received by at least two distinct platforms, such as TanDEM-X or HRWS, is defined as multistatic. Within this framework, addressing the design of single-pass multistatic InSAR missions is crucial for various scientific applications, particularly for the accurate generation of DEM through XTI-SAR [5], [6], [7]. While significant progress has been made in designing multistatic systems for future missions, not only in the SAR domain [19], [20], [21], [22], existing approaches mainly rely on the helix relative trajectory. On the one hand, the helix concept brings many advantages, such as the intrinsic passive safety of the close trajectory of the secondary around the primary satellite and the small amount of fuel for maintaining the stable close relative orbit [23], [24]. On the other hand, the helix configuration produces a time-varying baseline for SAR acquisition, which can affect the DEM [25]. Based on this consideration, we have recently proposed a different setup of the relative motion enabling fixed baselines, in parallel with the classical helix configuration, in order to achieve potential advantages in the DEM generation [26], [27].

In addition, most past and current SAR mission studies rely on space mission heritage for the orbit height selection in the classical range of 500–700 km, and few studies analyze the benefits of a very LEO region, as in [28]. This selection is commonly a tradeoff of many factors, such as the availability of the launch, the limitation on the lifetime, and the five-year re-entry regulation for LEO protected region clearance [29]. Few studies address the possibility of optimizing the orbit altitude (i.e., the orbit height) depending on the application, and even fewer studies are available for very low altitudes [28], [30]. The potential of reducing the orbit altitude is directly related to the possibility of employing SAR instruments with lower transmit power. Finally, the selection of the onboard engine technology for current InSAR studies is classically based on the chemical thruster heritage, providing impulsive control, as for TanDEM-X [13]. Such an approach, however, may be prone to lower control accuracy of the trajectory compared to other technologies, such as electric engines, which continuously produce the control force to maintain the reference trajectory [31], [32]. Thanks to such potential, there is an increasing interest in electric engines for future space studies, as they can improve the performance of the mission, depending on the specific application. Addressing the previous challenges is crucial for improving the performance of XTI-SAR and enabling new multisatellite configurations, also based on NewSpace approaches. This research aims to bridge the existing gaps in orbit height selection, multisatellite formation configuration, instrument transmission power, interferometric height accuracy, and onboard engine technology by providing an approach to address these challenges.

In light of these considerations, we propose a novel methodology to optimize the orbit altitude for multistatic XTI-SAR missions for DEM generation, scenario, i.e., where one satellite of the formation transmits the signal and at least two receive it (this can include the one transmitting or not). The model seeks to minimize the total energy required by the onboard engines and the SAR instrument. The approach is demonstrated through a design example considering three spacecraft flying in formation, which opens the possibility of a single-pass multibaseline XTI-SAR. The formation configuration is set up with a multiple-nested helix orbit to retain the passive safety of the satellite formation. Furthermore, the fixed-baseline concept is introduced and analyzed in combination with the helix geometry to identify the potential of this novel XTI-SAR mission mode.

This article is organized as follows. Section II describes the problem formulation, presenting the key concepts, variables, and parameters for a multistatic interferometric SAR mission. Section III presents the methodology, including the relative dynamical model and the guidance and control strategy for a generic formation flying configuration. Then, the optimal altitude analysis is derived, with the main performance parameters for optimal altitude selection to minimize the energy consumption of the system. Section IV discusses the results for two design examples, presenting the performance and considerations for different formation configurations. Finally, Section V concludes this article with a summary of the essential findings and an outlook on future research.

II. Problem Formulation

This work considers a satellite formation in LEO for DEM generation using single-pass XTI-SAR performing multistatic acquisitions. The initial layout is set up for the two-satellite case, with one main and one secondary spacecraft. The same approach can be adapted to the case of three or more satellites for multibaseline InSAR to resolve phase unwrapping errors and improve the DEM quality [33]. Starting from the approach in [13] and [18], we consider the following problem set-up.

1) A formation of two or more satellites in LEO.
2) A primary satellite flying at the center of the formation.
3) One or more secondary satellites.
4) Both the main and the secondary spacecraft are equipped with an SAR instrument.
5) Multistatic acquisition scenario, where one of the satellites transmits the signal and at least two satellites receive it (the transmitting satellite can also receive).
6) Two different formation configurations:
   a) helix relative trajectory [13], [18] and
   b) parallel relative trajectories to enable fixed baselines [26], [27].

In the context of a multistatic scenario, an acquisition plan is foreseen for TanDEM-X, where, for each acquisition, it

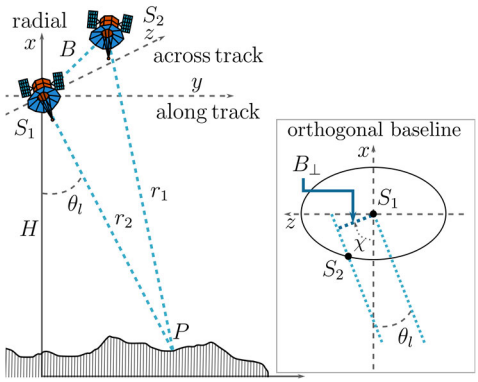

Fig. 1. InSAR geometry configuration for a two-satellite formation.

is decided which satellite is transmitting. One of the direct consequences of this assumption is the possibility to keep identical design of the platforms. To perform single-pass XTI-SAR, the instruments on different platforms observe the same area on the ground, and they are separated by a baseline with a component orthogonal to the direction of motion [6], [8], [34]. The joint processing of the two SAR images of the same area results in an interferogram, from which a DEM is obtained. Multiple interferograms can be combined to detect and correct phase unwrapping errors, following the approach in [35], or jointly processed according to the maximum likelihood principle [36]. In this way, a robust, high-quality DEM can be produced. Given these premises, the present work aims to provide a criterion for optimal altitude selection for XTI-SAR missions, considering different values for the interferometric baselines, instrument power demand, and electric engine technology.

In the following, we present the main assumptions and the main relationships among the performance figures for the analysis. First, we provide an overview of the main performance figures of a DEM, giving insights into the dependence of the DEM height accuracy on the baseline and orbit altitude. Second, we introduce a derivation to assess the power demand of the instrument, depending on the orbit altitude, under the assumption of imaging the same swath with the same geometric resolution. Then, Section II-A is dedicated to analyzing the main aspects that influence the absolute orbit design, such as the orbit altitude and the engine technology. Finally, we describe the reference system used for the relative motion of a formation flying.

Fig. 1 shows the basic geometry considered in this work. The primary and secondary satellites are identified with S_1 and S_2, respectively, in the local-vertical-local-horizontal reference frame $\{x, y, z\}$. This frame is centered in the main satellite, where the radial direction x points from the Earth center toward the main satellite, the across-track direction z is aligned with the angular momentum of the orbit of the main satellite, and the along-track direction y completes the right-hand side frame in the direction of motion. The distance between S_1 and S_2 is the interferometric baseline B. The look angle of the radar is identified by the angle θ_l, which is essential to identify the ranges r_1 and r_2 from each antenna to a generic point P. Finally, H represents the altitude of the primary satellite.

A. Height Accuracy and Resolution of DEM

This section presents an overview of the most relevant performance figures of a DEM. We consider the interferometric system in Fig. 1, with wavelength λ_w and range or chirp bandwidth B_r. The first important parameter for the interferometric analysis is the computation of the orthogonal baseline $B_\perp$, which is the projection of the baseline B on the direction perpendicular to the look direction in the radial-across-track plane, and can be expressed as

$$B_\perp = |B_x \sin\theta_l - B_z \cos\theta_l| \tag{1}$$

where θ_l is the look angle and B_x and B_z are the radial and across-track components of the baseline B. The orthogonal baseline is essential to evaluate many interferometric performance figures, as it relates to the standard deviation of the interferometric phase σ_φ to the standard deviation of the height σ_h (height accuracy) through the following relation:

$$\sigma_h = \frac{\lambda_w \, r \sin\theta_l}{2\pi B_\perp}\sigma_\varphi \tag{2}$$

where $r \cong r_1 \cong r_2$ is the slant range to the target. Multilooking the interferogram (e.g., by spatial averaging) allows for accuracy improvement at the expense of a degradation of the DEM resolution (or independent posting). The relation between the equivalent number of looks N_L and the correlation coefficient γ (or interferometric coherence) that can be used to obtain the standard deviation of the interferometric phase σ_φ can be found, e.g., in [2]. The Cramer–Rao bound relation provides an approximation of the standard deviation of the interferometric phase σ_φ highlighting its dependence on the number of looks and the interferometric coherence under the assumption of high coherence and a large number of looks [2]

$$\sigma_\varphi \cong \frac{1}{\sqrt{2N_L}}\frac{\sqrt{1-\gamma^2}}{\gamma}. \tag{3}$$

In addition, the 90th percentile of the height accuracy $\sigma_{h,90p}$ is also often used to characterize the DEM accuracy and can be approximated as [13]

$$\sigma_{h,90p} \cong 2.33 \cdot \sigma_h. \tag{4}$$

Furthermore, the geometric (or baseline) decorrelation, a multiplicative component of the interferometric coherence, is directly proportional to the ratio $B_\perp/r$ and inversely proportional to the wavelength λ_w, when the surface slope and misregistration can be neglected [9]. Most of the aforementioned performance figures depend on the baseline-to-range ratio $B_\perp/r$. Since the range r depends on the orbit altitude H and the look angle θ_l via geometrical correlation, the ratio of the orthogonal baseline to the orbit altitude $B_\perp/H$ plays an important role in the determination of the DEM performance.

B. Power Consideration for the SAR Instrument

Starting from the system in Fig. 1, we introduce a derivation to assess the power demand of the SAR instrument as a function of the orbit altitude, under the assumption of mapping the same swath with the same ground range and azimuth

resolutions and with the same noise-equivalent sigma zero (NESZ). Specifically, it is possible to identify a dependence of the power demand on the orbit altitude and derive an equation to connect this dependence. First, we consider an interferometric SAR system designed to operate at a reference altitude H_{ref}, with given DEM accuracy, DEM posting, and swath width. We assume that, by varying the altitude H, the aforementioned SAR system can still provide the same DEM performance and map the same swath and strip length in azimuth. According to the SAR theory, the range resolution is independent of the orbit height if the chirp bandwidth and the incidence angle are kept constant. Similarly, the azimuth resolution is also nearly independent of the orbit height, under the hypothesis that the antenna length is fixed. The slight variation of the azimuth resolution with height due to the spherical Earth geometry will be neglected in this work and could be compensated for by slightly adapting the processed Doppler bandwidth.

In general, we are interested in the required power of the antenna during data taking. The average radiated power P_{avg} is given by the product of and the radiated peak power P_{peak} and the instrument duty cycle ζ_{instr}

$$P_{\text{avg}} = P_{\text{peak}} \cdot \zeta_{\text{instr}}. \tag{5}$$

Then, the power demand during the transmission is computed from the average radiated power. In the power budget, it is important to consider the power losses due to the inefficiencies in the transmission chain through the transmission chain efficiency η_{tx}. The primary sources of such inefficiencies are the losses in the high-power amplifiers in the transmit-receive modules and the electronics components of the transmission chain. The power demand P_d needed by the instrument during data taking to achieve the required average radiated power P_{avg} is given by

$$P_d = P_{\text{avg}}/\eta_{tx}. \tag{6}$$

Considering TanDEM-X as an example, the radiated peak power is $P_{\text{peak}_{\text{ref}}} = 2260$ W, the instrument duty cycle is $\zeta_{\text{instr}} = 18\%$, and the efficiency of the transmission is $\eta_{tx} = 11\%$ [37]. The average radiated power is $P_{\text{avg}_{\text{ref}}} = 406.8$ W, and the power demand during data taking is approximately constant and equal to $P_d = 3.7$ kW. In this work, we neglect the power required when the instrument is not transmitting, considering a constant standby power with altitude. Further considering the orbit duty cycle ζ_{orbit}, the energy required per orbit is calculated as the energy needed during data taking

$$E_d = P_d \cdot T \cdot \zeta_{\text{orbit}} \tag{7}$$

where T represents the orbital period, given by

$$T = 2\pi \left(a^3/\mu\right)^{1/2} \tag{8}$$

where $\mu = 3.986 \times 10^5 \text{km}^3/\text{s}^2$ is the Earth's gravitational parameter, and a is the orbit semi-major axis. Considering the example of TanDEM-X, the energy required per orbit corresponds to $E_d = 175.29$ Wh, for an orbit duty cycle of $\zeta_{\text{orbit}} = 3\%$ and an orbital period T of 1.58 h.

For the purpose of this article, we are interested in assessing the power and the energy demand at different orbit altitudes. The approach adopted is based on the possibility of computing these quantities from the properties of a reference SAR system at a reference orbit altitude H_{ref}. Specifically, the reference values were considered from the TanDEM-X satellite, flying at an altitude $H_{\text{ref}} = 512$ km. From these reference values, the relation for the average radiated power P_{avg} at a generic altitude H has been derived as

$$P_{\text{avg}} = P_{\text{avg}_{\text{ref}}} \cdot \frac{H}{H_{\text{ref}}} \cdot \sqrt{\frac{R_\oplus + H_{\text{ref}}}{R_\oplus + H}} \tag{9}$$

where $R_\oplus$ is the Earth's mean equatorial radius. Specifically, we observe a reduction in the radiated power moving from the reference altitude to a lower height $H < H_{\text{ref}}$. To map the same swath from a lower height, in fact, a proportionally narrower antenna with a lower gain in both transmit and receive is required, and the NESZ has an inverse quadratic dependence on the gain. In addition, we should consider that the same NESZ is achieved with a far lower average transmit power when the orbit height is decreased; namely, the NESZ has a cubic dependence on the range and, therefore, on the orbit height. The combination of the inverse quadratic dependence due to the gain and the cubic dependence due to the range explains the term H/H_{ref}. Instead, the factor under the square root originates from the ratio of the different velocities at different orbital altitudes and is almost equal to one for altitudes in LEO. For example, considering the TanDEM-X values for the reference orbit height $H_{\text{ref}} = 512$ km and a radiated reference power $P_{\text{avg}_{\text{ref}}} = 406.8$ W, we obtain the average radiated power at different altitudes. For a lower altitude of 400 km, the average power demand reduces to 320 W, while increasing the altitude to 600 km, the corresponding average power rises to 473 W. Further assuming that the same azimuth strip length should be covered on the ground and that a shorter time (and duty cycle) is required for that at a lower altitude, we can compute the corresponding energy required by the SAR instrument per orbit

$$E_{d,H} = E_{d,\text{ref}} \cdot \frac{H}{H_{\text{ref}}} \cdot \sqrt{\frac{R_\oplus + H}{R_\oplus + H_{\text{ref}}}}. \tag{10}$$

Please note that constraining the length of the azimuth strip on the ground results in a change of the term under the square root between (9) and (10). Considering the example of TanDEM-X, reducing the altitude to 400 km results in a lower energy demand of 138 Wh, whereas increasing the altitude to 600 km results in a higher energy demand of 204 Wh. Under the previous assumptions, the relationships in (9) and (10) describe how the antenna power and energy demand vary depending on the altitude. To keep the same phase-to-height ratio, the orthogonal baseline should be scaled proportionally to the height, resulting in the same coherence loss due to baseline decorrelation.

C. Orbit Design

Following the derivation of the main performance figure for the SAR system, this section is devoted to analyzing the main aspects that influence the absolute orbit design. The mission design of multistatic interferometric SAR systems

TABLE I

DISTRIBUTION OF ORBIT ALTITUDE FOR PAST AND CURRENT MISSIONS CARRYING AN SAR SYSTEM

Orbit Altitude (km)	Number of objects (-)
< 400	5
$400 - 500$	23
$500 - 600$	97
$600 - 700$	26
> 700	20

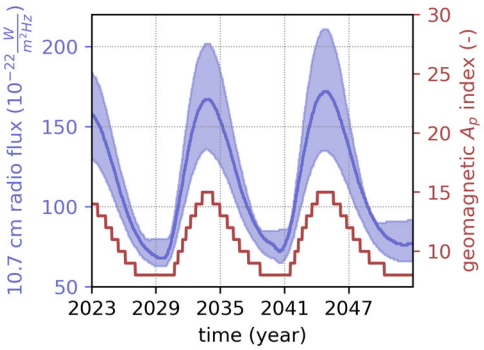

Fig. 2. Solar cycle prediction for the $F_{10.7}$ and A_p indexes, based on the Schatten model.

can be connected to three primary parameters: the orbit altitude, the baseline, and the number of satellites. Each one of them influences the orbit design and the interferometric performance. In this work, we consider a formation of two or more satellites, each mounting an SAR instrument, as shown in Fig. 1. The main satellite is at the center of the relative Cartesian frame, and the secondaries orbit around it. As mentioned in the introduction, few systematic studies analyze the optimal altitude for SAR applications, including considerations such as power demand, control effort, and propellant budget. Most current and past space missions devoted to SAR interferometry have been launched in LEO, in the altitude range (400 – 700) km and on quasi-circular sun-synchronous orbits (SSOs). Table I shows the altitude distribution of past and current space missions mounting an SAR system. About 170 space objects have been considered in the graph. The data have been retrieved from the ESA Database and Information System Characterizing Objects in Space (DISCOS) [40]. The graph shows that most SAR missions are in the LEO region. Few missions are at an orbital altitude below 500 km: the military USA 276 mission is one of the few at an orbital altitude of 400 km [41], while the Quill demonstration mission was one of the few SAR satellites flying below 300 km for a very short lifetime [42].

As introduced in Sections II-A and II-B, the orbit altitude influences the interferometric performance and the power demand of the SAR instrument during the transmission phase. Two further important aspects must be introduced during the mission design procedure. First, the mission lifetime is strictly connected with the orbit altitude due to the predominant effect of the atmospheric drag on the orbit decay at lower altitudes. Second, the control effort and, consequently, the propellant mass for orbit maintenance vary with the altitude and must

TABLE II

DISTRIBUTION OF AREA-TO-MASS RATIO VALUES FOR CURRENT AND PAST SPACE MISSIONS CARRYING AN SAR SYSTEM

Area-to-mass ratio (m^2/kg)	Number of objects (-)
< 0.005	71
$0.005 - 0.010$	51
$0.010 - 0.020$	22
$0.020 - 0.025$	27
> 0.025	4

be considered when designing a future mission. The effect of the atmospheric drag becomes more severe as the altitude decreases, and it strictly depends on solar activity. In this work, we consider the Schatten model for the solar cycle prediction, characterized by two indices: the 10.7 solar radio flux or $F_{10.7}$ index, which is the noise level generated by the Sun, and the geomagnetic A_p index, which represents the general level of electromagnetic activity over the globe for a given day [38]. Fig. 2 illustrates the evolution of the solar cycle prediction between 2023 and 2053. We can observe that maximum conditions repeat with a cycle of about 11 years. These predictions are essential to compute the time variation of the atmospheric density ρ, as function of altitude and time. We adopted the NRLMSISE empirical model of the atmosphere, incorporating the information on A_p and $F_{10.7}$ [39], to define the atmospheric density as a function of the altitude $\rho = \rho(H)$. In addition, the effect of atmospheric drag depends on the altitude and the physical parameters of the satellites. Notably, the acceleration imparted by the drag is proportional to the area-to-mass ratio of the vehicle

$$a_{\text{drag}} = -0.5\rho C_D \frac{S}{m} v^2 \tag{11}$$

where ρ is the atmospheric density, C_D is the drag coefficient (generally in the range 2.2–3.1). The area-to-mass ratio S/m represents the ratio between the cross-sectional area in the direction of motion and the spacecraft mass, and the quantity v represents the spacecraft's velocity. The ratio S/m is critical to assess the effect of the atmospheric drag on the absolute orbit evolution in time, and it depends on the physical characteristics of the space platform. The ESA DISCOS database provides information on the mass and cross-sectional area of current and past space missions [40]. Table II shows the distribution of the area-to-mass ratio for current and past SAR missions: the majority of satellites have a ratio S/m smaller than 0.01 m^2/kg. Understanding of the most common range of this parameter is fundamental for evaluating the typical effect of the atmospheric drag on the dynamical motion. In addition, a control strategy based on a propulsive system is implemented to compensate for the external orbital perturbations. The control effort and, consequently, the propellant mass mainly depend on the engine technology and the control strategy. We selected electric thruster technology to ensure more accurate trajectory control against external perturbations, such as gravitational potential field, atmospheric drag, and solar radiation pressure. The advantages of electric thrusters are the precise continuous control against deviation from the

nominal trajectory and a reduced mass of propellant on board, thanks to the higher specific impulse compared to chemical technology. This aspect is derived from the well-known Tsiolkovsky equation, which provides a relation between the spacecraft mass and the propellant mass

$$m_p = m_0 \left(1 - e^{\frac{-\Delta v}{I_{sp} g_0}}\right) \tag{12}$$

where m_p is the propellant mass, m_0 is the spacecraft's initial mass, I_{sp} is the engine specific impulse, g_0 is the gravitational acceleration (i.e., 9.81 m/s^2), and Δv is the change of velocity of the satellite. Note that the specific impulse I_{sp} is a measure of how efficiently a reaction mass engine generates thrust. Its values are typically 150–300 s for chemical thrust, and 1500–3000 s for electric propulsion [32]. The efficiency of electric engines becomes an advantage in reducing the mass of propellant on board for the same Δv of a chemical thruster. On the other hand, we have to deal with some limitations of the electric engines. First, the thrust level, typically in the range 0.01 − 100 mN [32], is much lower than that of chemical propulsion and, consequently, the time for maneuvering increases. In addition, they have a more demanding requirement from the power point of view, proportional on the thrust level, typically in the range of 200–700 W [32]. This second aspect is crucial to evaluate the feasibility of the mission, and it is included in the optimization procedure of Section III.

D. Relative Trajectory and Baseline Definition

This section presents the fundamental parameters to describe the relative motion. As shown in Section II-A, one essential aspect of single-pass multisatellite XTI-SAR is the baseline definition. Its value and evolution in time depend on the relative trajectory among the main and secondary satellites. We have identified two possible scenarios based on the analysis in [26]. The first one consists of a relative trajectory based on the natural solution of the unperturbed relative motion, e.g., the helix trajectory. This solution results in a time-varying baseline, as for the TanDEM-X configuration [13]. The second option consists of a relative trajectory under a fully forced relative motion to obtain a fixed baseline in time. This second configuration requires continuous control of the relative trajectory against the natural dynamics to keep a constant baseline [26]. Due to the nature of continuous thrust, this second scenario is far more expensive in terms of control effort and propellant mass for the mission lifetime, whereas the helix configuration requires the control force only to compensate for external orbital perturbations [27].

To adequately describe the relative motion, the absolute orbit of the main satellite is identified by nonsingular Keplerian elements $\boldsymbol{el}_c = \{a, \lambda, e_x, e_y, i, \Omega\}_c$. Similarly, the nonsingular Keplerian elements of the N secondary satellites are identified by the index j, with $j = 1, \ldots, N$, as $\boldsymbol{el}_j = \{a, \lambda, e_x, e_y, i, \Omega\}_j$. The quantity a is the semi-major axis, $\lambda = \omega + M$ is the mean argument of latitude depending on the argument of perigee ω and the mean anomaly M, i is the orbit inclination, Ω is the orbit right ascension of the ascending node, and $\{e_x, e_y\}$ are the x and y components of the eccentricity vector, $e\cos\omega$ and $e\sin\omega$, respectively. From this representation, the relative motion of the j-th secondary around the primary can be described by the quasi-nonsingular mean relative orbital elements (ROEs) [23]

$$\boldsymbol{\delta\alpha}_j = \begin{Bmatrix} \delta a \\ \delta\lambda \\ \delta e_x \\ \delta e_y \\ \delta i_x \\ \delta i_y \end{Bmatrix}_j = \begin{Bmatrix} (a_j - a_C)/a_C \\ \lambda_j - \lambda_C + (\Omega_j - \Omega_c)\cos i_c \\ e_{x_j} - e_{x_c} \\ e_{y_j} - e_{y_c} \\ i_j - i_c \\ (\Omega_j - \Omega_c)\sin i_c \end{Bmatrix} \tag{13}$$

where δa_j is the relative semi-major axis, $\delta\lambda_j$ is the relative mean argument of latitude, δe_{x_j} and δe_{y_j} are the x and y components of the relative eccentricity vector $\boldsymbol{\delta e_j}$, whereas δi_{x_j} and δi_{y_j} are the x and y components of the relative inclination vector $\boldsymbol{\delta i_j}$. To connect the ROE description with the Cartesian representation, we adopt a first-order linear mapping into relative Cartesian coordinates $\{x, y, z, v_x, v_y, v_z\}$

$$\begin{cases} \dfrac{x}{a_c} = \dfrac{\delta a}{a_c} - \delta e_x \cos u - \delta e_y \sin u \\ \dfrac{y}{a_c} = -\dfrac{3}{2}(\lambda_c - \lambda_0)\dfrac{\delta a}{a_c} + \delta\lambda + 2\delta e_x \sin u - 2\delta e_y \cos u \\ \dfrac{z}{a_c} = \delta i_x \sin u - \delta i_y \cos u \\ \dfrac{v_x}{v_c} = \delta e_x \sin u - \delta e_y \cos u \\ \dfrac{v_y}{v_c} = -\dfrac{3}{2}\dfrac{\delta a}{a_c} + 2\delta e_x \cos u + 2\delta e_y \sin u \\ \dfrac{v_z}{v_c} = \delta i_x \cos u + \delta i_y \sin u \end{cases} \tag{14}$$

where v is the circular velocity of the primary satellite, $u = nt$ with n the mean motion and t the time. The mean motion is defined as $n = (\mu/a^3)^{1/2}$, with μ the gravitational parameter. From the first order linear mapping into relative Cartesian coordinates, the orthogonal baseline $B_\perp$ is obtained as a linear combination of the vertical (radial) and horizontal (across-track) components of the relative trajectory for a given radar look angle θ_l, as in (1). For a two-satellite formation, the selection of the orthogonal baseline for XTI-SAR is usually driven by the height of ambiguity and limited by phase unwrapping. If multiple baselines are available, the largest baseline can be selected to maximize the height accuracy of the DEM, trading off the effect of baseline decorrelation and phase-to-height scaling. In this analysis, we do not consider that two or more images can be filtered to a common band to avoid volume decorrelation at the expense of a reduction of the range resolution and therefore of the number of looks for the same DEM posting [43], as we expect this does not significantly impact the final results.

Finally, depending on the value of the baselines, we obtain different separations among the satellites, and this could impact the control effort in terms of velocity variation Δv imparted by the engine. For example, considering the TanDEM-X configuration, the impulsive Δv imparted to control the formation is linearly proportional to the satellite separation [23]. An increment in the Δv corresponds to an increment in the control acceleration, and, for the same satellite mass, to a higher thrusting level and power demand of the

engine. Specifically, input electrical power P_{in} is a function of the thrust level F_t, the thrust efficiency η, and the specific impulse I_{sp} [44]

$$\frac{P_{\text{in}}}{F_t} = \frac{g_0 I_{sp}}{2\eta} \tag{15}$$

where the thrust F_t can be computed from the knowledge of the control acceleration and the satellite mass properties.

III. Methodology

The most important outcome of Section II is the impact of both the baseline and the orbit altitude on different mission design aspects. Depending on H and $B_\perp$, we can identify a specific energy requirement, depending on the payload demand, propulsive technology, and orbital parameters. This section presents a novel procedure for defining a criterion for the orbit altitude selection, based on the minimization of the overall power demand and propulsion effort. During the derivation, we account for the different considerations presented in Section II. In addition, we assume an ideal orbit navigation with no error in the absolute and relative position reconstruction. This aspect should be included in the model formulation during the mission design procedure for a precise control routine assessment.

A. Relative Dynamical Model

This section describes the relative dynamical model of distributed space systems. Similar to the Hill–Clohessy–Wiltshire (HCW) equations [45], we retain the assumption of a quasi-circular orbit of the primary satellite. On the other hand, we include the effect of the main external perturbation for the LEO region in the dynamics. We adopt a dynamic representation based on ROE to include the differential mean Earth's oblateness J_2 and atmospheric drag. In a first approximation, the effect of the differential drag is described by the drift in the relative semi-major axis $\delta\ddot{a}$, which can be considered together with the ROE components in an augmented state $\boldsymbol{\delta a^*}$ [46]

$$\boldsymbol{\delta a^*} = \left\{\delta a, \delta\lambda, \delta e_x, \delta e_y, \delta i_x, \delta i_y, \delta\ddot{a}\right\}. \tag{16}$$

Note that we have neglected the differential drift in the relative eccentricity components $\delta\ddot{e}_x$ and $\delta\ddot{e}_y$. The resulting equations of motion are the following:

$$\begin{aligned} \boldsymbol{\delta\dot{\alpha}^*}(t) &= \boldsymbol{A}(t, t_0)\,\boldsymbol{\delta\alpha^*}(t_0) \\ \boldsymbol{A}(t, t_0) &= \left(\boldsymbol{A_{hcw}}(t) + \boldsymbol{A_{j2,dd}}(t)\right) \end{aligned} \tag{17}$$

where the matrix $\boldsymbol{A_{hcw}}$ includes the unperturbed contribution from the HCW equations, whereas the matrix $\boldsymbol{A_{j2,dd}}$ includes the effect of the Earth's oblateness and differential drag perturbation. The first term is represented by

$$\boldsymbol{A_{hcw}}(t) = \left[\begin{array}{c|c} 0 & \mathbf{0}_{2\times 5} \\ -1.5\,n & \\ \hline \mathbf{0}_{4\times 1} & \mathbf{0}_{4\times 5} \end{array}\right] \tag{18}$$

where the quantity $\mathbf{0}_{d_r\times d_c}$ is a matrix full of zeros with dimensions $\{d_r, d_c\}$, t is the time variable, and n is the mean motion of the primary orbit. The component, including the effects of J_2 and differential drag is defined as

$$\boldsymbol{A_{j2,dd}}(t) = \left[\begin{array}{c|c} \mathbf{A_{j2}}(t) & \mathbf{A_{dd}}(t) \\ \hline \mathbf{0_{1\times 6}} & 1 \end{array}\right] \tag{19}$$

where $\mathbf{A}_{j2}$ is the part including the Earth's oblateness effect, and it was derived from [46]

$$\mathbf{A}_{j2} = k\begin{bmatrix} 0 & 0 & 0 & 0 & 0 & 0 \\ -\frac{7}{2}EP & 0 & e_xGFP & e_yGFP & -FS & 0 \\ \frac{7}{2}e_yQ & 0 & A_{3,3} & A_{3,4} & 5e_yS & 0 \\ -\frac{7}{2}e_xQ & 0 & A_{4,3} & A_{4,4} & -5e_xS & 0 \\ 0 & 0 & 0 & 0 & 0 & 0 \\ \frac{7}{2}S & 0 & -4e_xGS & -4e_yGS & 2R & 0 \end{bmatrix}. \tag{20}$$

The complete expression of each term of the matrix is obtained from [46] and adapted for the case of a quasi-circular orbit of the primary satellite using the following expressions for the parameters (where $\varrho = 1$):

$$\begin{aligned} &E = 1 + \varrho; && F = 4 + 3\varrho; \\ &P = 3\cos^2(i) - 1; && S = \sin(2i); \quad R = \sin^2(i); \\ &Q = 5\cos^2(i) - 1; && G = 1/\varrho^2; \quad \dot{\omega} = kQ; \\ &k = \frac{3}{4}\frac{J_2 R_\oplus^2\sqrt{\mu}}{a^{7/2}\varrho^4}; && \omega_f = \omega + \dot{\omega}t; \\ &A_{3,3} = -4e_xe_yGQ; && A_{3,4} = -\left(1 + 4Ge_y^2\right)Q; \\ &A_{4,3} = \left(1 + 4Ge_x^2\right)Q; && A_{4,4} = 4e_xe_yGQ. \end{aligned}$$

The second part of (19) is connected to the differential drag, i.e., $\mathbf{A}_{dd}$, and it was derived by [46] following the density model free formulation:

$$\mathbf{A}_{dd}(t) = \begin{bmatrix} 1 \\ \mathbf{0}_{5,1} \end{bmatrix}. \tag{21}$$

The selected model is able to provide an accurate representation of the dynamics, independently of the distance among the satellites in the formation, as demonstrated in [46].

B. Guidance and Control Strategy

This section defines the strategy for the formation control to keep the spacecraft on the reference relative trajectory and to compensate for external perturbations. First, to maintain the proper configuration for SAR acquisition, we consider a continuous control to compensate for the natural oscillation of the relative trajectories under external perturbations. The guidance is set equal to the trajectory for the case of no external perturbations, i.e., the ideal trajectory for SAR acquisition

$$\boldsymbol{\delta\dot{\alpha}_{ref}}(t) = \boldsymbol{A_{hcw}}(t)\,\boldsymbol{\delta\alpha_{ref}}(t_0) \tag{22}$$

where $\boldsymbol{\delta\alpha_{ref}}(t_0)$ is the reference trajectory at the initial time instant. Subsequently, we derive the control strategy. Continuous control is envisioned to keep the desired across-track separation, obtained with low-thrust engines, such as ion or hall thrusters. We identify two primary objectives of the control: keep the orbit altitude against the natural decay due to atmospheric drag (see Section II-C), and maintain the

secondary spacecraft on the reference trajectory around the primary, in the presence of external perturbations. In this analysis, we have not included the control effort to compensate for other effects on the absolute orbit due to external perturbations, such as nodal drifting and inclination variation. Two different strategies have been implemented to assess the magnitude of the control effort for the two objectives. First, an analytical derivation of the control acceleration is carried out to estimate the order of magnitude of the control. Subsequently, a numerical implementation with a closed-loop control is presented to properly include the effects of the external perturbations in the control effort.

1) Semi-Analytical Control Strategy: In the first approximation, the control effort to keep the absolute orbit altitude of a satellite is computed directly from the acceleration imparted by the atmosphere on the platform [see (11)]. Consequently, to assess the velocity variation Δv_{abs} to keep the altitude H over a certain time Δt, the system needs to produce an acceleration with the same magnitude as (11), but in the opposite direction

$$\Delta v_{\text{abs}}^{\text{analytical}} = \left| -a_{\text{acc,drag}} \Delta t \right| \tag{23}$$

where the quantity $|\cdot|$ indicates the absolute value. Similarly, a first approximation of the control effort to keep the relative motion can be identified for different formation configurations. For the case of helix orbit, as in TanDEM-X, a good estimation of the velocity variation Δv_{rel} to maintain the relative motion was provided in [23]

$$\Delta v_{\text{rel}}^{\text{analytical}} = \left| \frac{v}{2} \delta \, e\dot{\varphi} \, \Delta t \right| \tag{24}$$

where v is the velocity of the secondary satellite, δe is the magnitude of the relative eccentricity vector [see (13)], and $\dot{\varphi}$ represents the effect of J_2 on the relative motion

$$\dot{\varphi} = \frac{3}{2} \frac{\pi J_2}{T} \left(\frac{R_\oplus}{a_c} \right)^2 \left(5 \cos^2 i_c - 1 \right) \tag{25}$$

where T is the orbit period of the main satellite.

As introduced in Section I, this article also investigates the possibility of setting up fixed-baseline configurations among the satellites in the across-track direction, similar to the analyses presented in [26]. In order to maintain a fixed separation across-track, the relative position of the secondary is continuously controlled in the radial-across-track plane against the natural oscillations of the relative dynamics. Starting with the linear description of the relative motion in the absence of external perturbation [i.e., the HCW dynamics in (22)], we solve the system in terms of control acceleration components when the separation in radial and across-track direction is kept constant, and no along-track separation is present [26]. For this condition, the acceleration imparted to the secondary is approximated as

$$\begin{cases} a_{\text{acc},x} = -3n^2 x_0 \\ a_{\text{acc},y} = 0 \\ a_{\text{acc},z} = n^2 z_0 \end{cases} \tag{26}$$

where the quantities x_0 and z_0 represents the separation in the radial and across-track direction, respectively, i.e., the radial and across-track components of the baseline B, defined in (1) as B_x and B_z. This solution is obtained for a system that maintains the initial radial and across-track separations constant in time, against the natural oscillations of the relative motion. As can be observed in (26), maintaining a fixed separation in the radial direction is three times more expensive than a separation across-track. This means that, for typical look angles of InSAR systems, the same orthogonal baseline is achieved from a separation in the across-track direction with a smaller effort in terms of velocity variation

$$\Delta v_{\text{rel}}^{\text{analytical}} = \left| a_{\text{acc},x} \Delta t \right| + \left| a_{\text{acc},z} \Delta t \right| . \tag{27}$$

Note that the derivation presented in this paragraph is only a first estimate of the control effort. A more refined analysis is obtained by implementing the closed-loop control strategy.

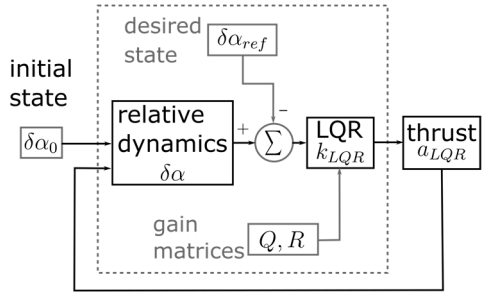

Fig. 3. LQR control logic for a single spacecraft.

2) Closed-Loop Control Strategy: Following the semi-analytical procedure, we derived a numerical closed-loop control strategy for a more accurate assessment of the control effort. In this case, we included both the Earth's oblateness and the atmospheric drag perturbations in the equations of the dynamics. The control is described in the Cartesian frame as acceleration components $\boldsymbol{a_{acc}}(t) = \{a_{\text{acc},x}, a_{\text{acc},y}, a_{\text{acc},z}\}(t)$. To include the control effort in the ROEs state space representation of the dynamics [see (17)], the control matrix $\hat{\boldsymbol{B}}_{\boldsymbol{c}}$ is introduced. Starting from the linearized equations of the dynamic, we get the following system:

$$\boldsymbol{\delta\dot{\alpha}}^* (t) = \boldsymbol{A} \, (\mathrm{t,t_0}) \, \boldsymbol{\delta\alpha}^* (t_0) + \hat{\boldsymbol{B}}_{\boldsymbol{c}} \, (t, t_0) \, \boldsymbol{a_{acc}}(t) \tag{28}$$

where $\hat{\boldsymbol{B}}_c(t)$ is the control matrix for the linearized equations of the relative motion [47]

$$\hat{\boldsymbol{B}}_{\boldsymbol{c}} \, (t) = \frac{1}{n a_c} \begin{bmatrix} 0 & 2 & 0 \\ -2 & 0 & 0 \\ \sin u & 2\cos u & 0 \\ -\cos u & 2\sin u & 0 \\ 0 & 0 & \cos u \\ 0 & 0 & \sin u \end{bmatrix} . \tag{29}$$

The control logic is based on the linear quadratic regulator (LQR) controller. The control aims to maintain the desired formation geometry, operating the system at the minimum cost. Linear quadratic controllers have been used in different works involving formation flying [48], [49], and the control logic is represented in Fig. 3. The guidance provides the reference trajectory, and the semi-analytical estimation of the control provides the nominal control profile. The initial

conditions of the distributed system are propagated using the dynamical model in (28) to compute the actual state, including the contribution of the external perturbations. The error between the actual state and the guidance trajectory is computed at each time step. This control logic assumes that only the deputies perform manoeuvres to keep the guidance relative trajectory around the chief. The control error and the corresponding control action have been computed for each couple of deputy j–chief satellites. Hence, the optimal control is tailored for every single element of the formation.

The error is used to design the optimal gains of the LQR controller, which provide the feedback control to the system dynamics. The aim of the LQR is to minimize the error between the actual $\boldsymbol{\delta\alpha}$ and the reference state $\boldsymbol{\delta\alpha}_{\text{ref}}$

$$\lim_{n\to\infty} \boldsymbol{\delta\alpha} - \boldsymbol{\delta\alpha}_{\text{ref}} = 0 \tag{30}$$

where the quantity $\boldsymbol{\delta\alpha} - \boldsymbol{\delta\alpha}_{\text{ref}}$ defines the error, and it is equal to the variable $\boldsymbol{x}_e$. Following the LQR theory, the optimal control acceleration $\boldsymbol{a}_{\text{LQR}} = -\boldsymbol{k}_{\text{LQR}}\boldsymbol{x_e}$ is based on the computation of the gain matrix $\boldsymbol{k}_{\text{LQR}}$, via the minimization of the following quadratic cost function:

$$J = \frac{1}{2}\int_{t_0}^{t_f} \left(\boldsymbol{x}_e^{\text{T}}\boldsymbol{Q}\boldsymbol{x}_e + \boldsymbol{a}_{\boldsymbol{acc}}^{t}\boldsymbol{R}\boldsymbol{a}_{\boldsymbol{acc}}\right) \tag{31}$$

where the matrices $\boldsymbol{Q}$ and $\boldsymbol{R}$ represent the state gain matrix and the control effort matrix, respectively. The matrix $\boldsymbol{Q}$ is symmetric and positive semi-definite, while $\boldsymbol{R}$ is symmetric and positive definite.

Equation (31) represents the infinite-time LQR quadratic cost function, which provides different convergence durations depending on the selection of the control weights. The optimal feedback gain is provided by solving the Riccati equation, and it is given by

$$\boldsymbol{a}_{\text{acc,LQR}}(t) = -\boldsymbol{R}^{-1}\hat{\boldsymbol{B}}^{\text{T}}\boldsymbol{P}^{\text{T}}\boldsymbol{x}_e + \boldsymbol{a}_{\text{acc,ref}} \tag{32}$$

where the matrix P comes from the solution of the Riccati equation

$$\dot{\boldsymbol{P}}(t) = -\boldsymbol{P}(t)\boldsymbol{A}(t) - \boldsymbol{A}^{T}(t)\boldsymbol{P}(t) - \boldsymbol{Q} + \boldsymbol{P}\hat{\boldsymbol{B}}\boldsymbol{R}^{-1}\hat{\boldsymbol{B}}^{\text{T}}\boldsymbol{P}(t). \tag{33}$$

The time dependence for the case under analysis only depends on the time variation of the plant matrix of the relative motion, which includes the effects of differential drag and mean J_2. The matrices $\boldsymbol{Q}$ and $\boldsymbol{R}$ were chosen after a parametric analysis and set equal to

$$\begin{aligned}\boldsymbol{Q} &= \text{diag}\,[1, 1, 1, 1, 5, 5]\\ \boldsymbol{R} &= \text{diag}\,[1, 1, 1]\,.\end{aligned} \tag{34}$$

We recover the velocity variation from the optimal control on, corresponding to the reference trajectory maintenance, by multiplying the control acceleration components for the discretization time of the simulation dt. In addition, depending on the spacecraft mass, it is also possible to compute the corresponding thrust level as $F_t = a_{\text{acc},LRQ}m_{sc}$, with m_{sc} being the mass of the platform. This is fundamental to include the maximum acceleration that the thruster technology can provide as a limitation to the optimal thrust obtained with the LQR controller, and at the same time, the power demand of the electric engine.

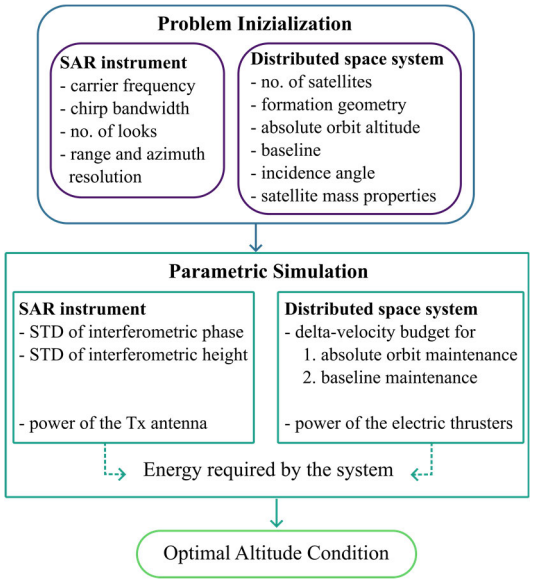

Fig. 4. Step-by-step procedure for the identification of the minimum altitude condition for each $B_\perp/H$ ratio.

C. Optimal Altitude Analysis

Fig. 4 shows the step-by-step procedure used to identify the optimal altitude condition for each $B_\perp/H$ ratio. First, we initialize the problem, then we perform the parametric simulation, considering the orbit altitude and the baseline-to-altitude ratio as fundamental parameters. Finally, we compute the power required by the system, and we define which one is the optimal altitude condition to minimize the energy cost and keep the desired interferometric performance.

1) Problem Initialization: During the initialization of the scenario, we select the input parameters for the SAR instrument. Concerning the carrier frequency f, we consider the exemplary case of Ka-band (f = 35.75 GHz). The selection of the Ka-band is based on the reduced penetration in the terrain of the electromagnetic wave and, at the same time, the opportunity to achieve good interferometric performance with small baselines (<100 m), due to the dependence of the height of ambiguity on the wavelength. The former aspect is important for obtaining observations that are less affected by the penetration and therefore a more accurate DEM [1]. Still, the proposed approach is general and can be transferred or adapted to different frequency bands. Depending on the desired range resolution, the system or chirp bandwidth has to be selected. Similarly, the look angle θ_l influences the SAR performance and the orthogonal baseline computation. Then, we select the desired range and azimuth resolution for dimensioning the antenna. In addition, we assume a system with the same posting, swath width, antenna length, and pulse repetition frequency (PRF). With a change in altitude, for example, a reduction, to map the same swath from a lower height, a proportionally narrower antenna with a lower gain is used, and the same NESZ is achieved with a lower peak and average transmit power. In parallel with the dimensioning of the SAR system, we initialize the distributed space system, setting the number of satellites N, and their physical

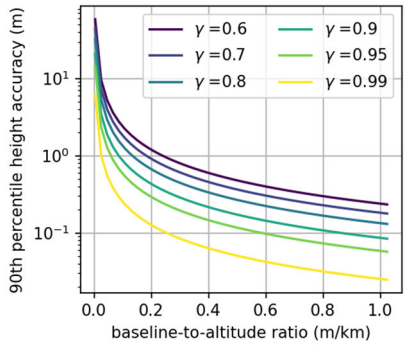

Fig. 5. Height accuracy (90th percentile) $\sigma_{h,p90}$ for variable baseline over altitude ratio and coherence levels, with 52 looks.

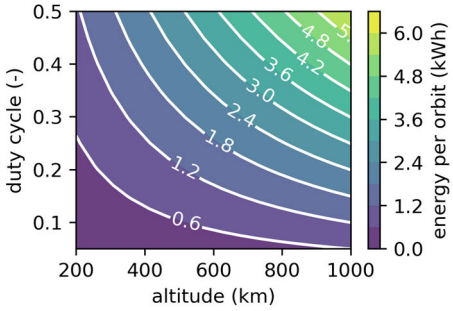

Fig. 6. Energy requirement (per orbit) of the SAR instrument for different orbit duty cycles and orbit altitudes.

properties (spacecraft mass m and cross-sectional area S). These parameters influence the magnitude of the atmospheric drag on the spacecraft's dynamics.

As described in Section II-C, we can identify two main common ranges for the S/m ratio: satellites with S/m in the order of 0.005 m^2/kg and satellites with S/m in the order of 0.025 m^2/kg. The former is representative of some exemplary missions, such as the Swarm mission by ESA and the TanDEM-X mission; the latter is, for example, representative of the SMOS mission by ESA. To minimize the differential effect of the atmospheric drag on the relative motion, we assumed that the S/m is the same for all the satellites in the formation. As discussed in Sections I and II, we identify the following scenario. A multistatic system based on nested helix relative trajectories. The chief satellite is at the center (origin) of the formation. The deputies fly around the chief on relative helix trajectories, similar to TanDEM-X. A multistatic acquisition scenario is considered, where one of the satellites transmits the signal and at least two receive it. Note that within the transmission plan, the transmission role can be exchanged among the satellites in the formation, keeping the mission flexible and balanced from an energy consumption point of view.

2) Parametric Simulation: A parametric simulation is carried out in terms of varying altitude H and orthogonal baseline $B_\perp$. Starting from the SAR parameters and the desired resolution, we identify the expected coherence, including the system and baseline decorrelations. The coherence γ is used for evaluating the standard deviation of the interferometric

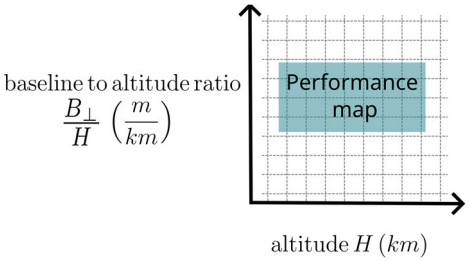

Fig. 7. Example of a performance map for the representation of each performance index.

phase σ_ψ, and consequently, the standard deviation of the interferometric height σ_h. Fig. 5 represents the 90th percentile of the interferometric height error, considering an SAR system with f = 35.75 GHz, B_r = 100 MHz, number of looks equal to 52, and $\theta_l = 35°$. The figure shows how the height accuracy improves with higher $B_\perp/H$ ratios and higher coherence levels. In addition, to maintain constant performance, one possibility is to keep a constant ratio $B_\perp/H$ and a constant NESZ. Note that the accuracy of the DEM will also be constant if a specific posting is considered. The SAR instrument input power is computed with the procedure in Section II-B, as a function of the orbit altitude and the NESZ. Different orbit duty cycles, from 5% to 50% of one orbit period, were considered. In the computation of the instrument input power, we assume that the geometric decorrelation remains the same for a fixed baseline-to-altitude ratio. Consequently, we consider only the influence of the altitude on the instrument input power. The energy required per orbit E_d by the SAR instrument is shown in Fig. 6 for an altitude range of (200, 1000) km. The energy demand increases with the altitude and the orbit duty cycle, as predicted in the model [see (9)]. Consequently, the instrument power demand would greatly benefit from a reduction in the orbit altitude for the same orbit duty cycle. However, the latter aspect is connected with the observation period of the SAR instrument over one orbit period, and, ideally, a higher orbit duty cycle allows for a larger data volume and better coverage of the imaged area. These two aspects should be balanced during the mission design.

3) Parametric Maps as a Function of Altitude and Interferometric Baseline: Multiple maps have been generated to represent the delta-velocity budget and the energy budget for the multistatic system to assess the combined impact of the control for formation maintenance and the energy required for transmission. Each map represents the optimal condition for the maneuvering satellite in each chief-deputy couple. The performance maps are generated in terms of two parameters: the orbit altitude H, and the baseline-to-altitude ratio $B_\perp/H$, as depicted in Fig. 7. Note that the y-axis reports the value of the ratio between the orthogonal baseline and the altitude in terms of (m/km): for an altitude of 400 km and a ratio of 0.2 m/km, we obtain an orthogonal baseline of 80 m. When considering the case of nested helix orbit, the interferometric baselines coming from the maps represent the value of the baseline at the initial time step, and it varies in time due to the time evolution of the helix geometry. The approach followed in the analysis is as follows. First, the procedure evaluates the

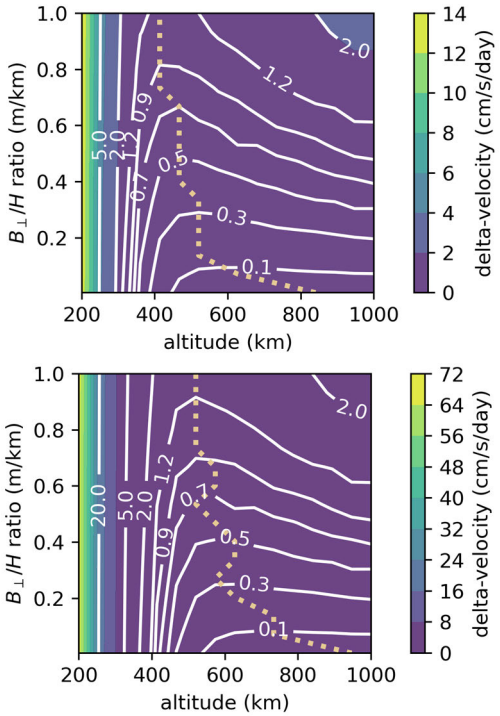

Fig. 8. Daily velocity variation Δv for absolute and relative orbit maintenance. Helix relative trajectory with S/m = 0.005 m^2/kg (top) and S/m = 0.025 m^2/kg (bottom).

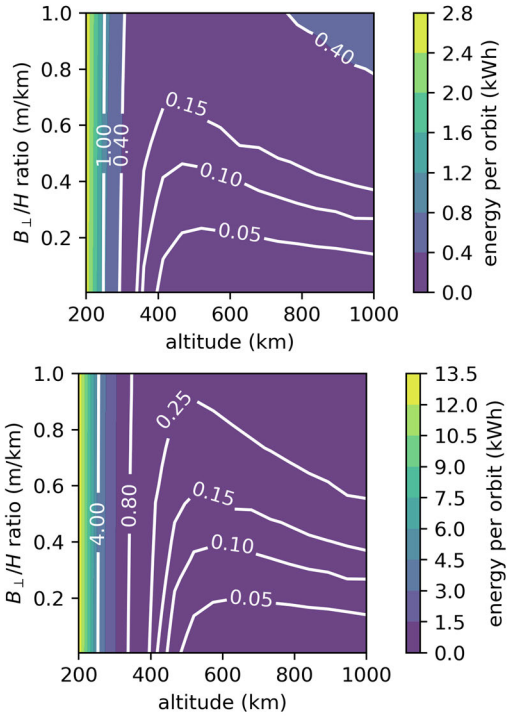

Fig. 9. Energy (per orbit) required by the electric engine for absolute and relative orbit maintenance. Helix trajectory with: S/m = 0.005 m2/kg (top), S/m = 0.025 m2/kg (bottom).

velocity variation required for one day to keep the formation configuration. The methodology described in Section III-B is used to compute the combined control effort for absolute orbit maintenance, as well as for perturbing effects correction of the relative trajectory with the closed-loop numerical simulator. Considering the scenario described in Section III-C1, Fig. 8 shows the delta-velocity required to control the formation over one day. The Δv is reported for each manoeuvering satellite, namely, the deputy j.

The control cost Δv is evaluated for two area-to-mass ratios S/m: 0.005 m^2/kg (top graph) and 0.025 m^2/kg (bottom graph). In addition, the minimum delta-v condition for each $B_\perp/H$ ratio is represented by the yellow dotted line. As expected, higher S/m ratios are more affected by the atmospheric drag at lower altitudes. Moreover, we observe how the control effort increases for large baseline-to-altitude ratios and low altitudes (below 400 km), due to the higher atmospheric drag effect. For high orbit altitude, instead, the predominant contribution to the control is given by the formation maintenance, as the effect of the drag decreases almost exponentially with the altitude.

After the generation of the maps in terms of delta-velocity, we are also interested in evaluating the energy required by the electric engine. From the knowledge of the control acceleration level needed by the controller and the satellite mass, the required acceleration poses a requirement for the thrust level that the electric engine should be able to guarantee continuously. Then, the engine input power is computed from the thrust level, the engine specific impulse, and the engine efficiency. The resulting energy required per orbit by the electric engine is shown in Fig. 9, where we considered a satellite with a mass of 125 kg and a Hall effect thruster with a specific impulse of 2500 s and an efficiency of 0.4. To account for the preliminary design of the propulsive system, we add a 40% margin on the thrust level required by the controller. The maps in Fig. 9 exhibit a similar behavior to the delta-velocity maps, with higher requirements at lower altitudes, and a dependence on the $B_\perp/H$ ratio at higher altitudes. The third step in the procedure is the computation of the combined energy requirement, considering the contribution of the electric engine and the transmitting instruments for different values of the orbit duty cycle.

The aim of the analysis is to identify the altitude that minimizes the energy demand. In this work, we do not assess the impact of the altitude on the energy used by other subsystems, as this is dependent on the specific scenario and would imply strong assumptions. Given the SAR instrument and the electric engine power requirements, we compute the combined energy demand per orbit for the system. First, increasing values of the orbit duty cycles for the SAR instrument have been considered: 5%, 15%, 25%, and 50%. Then, the combined energy per orbit is computed as

$$E_{s/c} = E_d + E_{\text{in}} \tag{35}$$

where E_d is the energy demand of the SAR instrument from (10), and E_{in} is the energy demand of the electric engine (from maps in Fig. 9). During this analysis, we assume a constant power demand over the altitude for the other subsystems of the spacecraft, e.g., the attitude control system, the onboard computer, etc. Consequently, we have not included this term in the optimal altitude analysis.

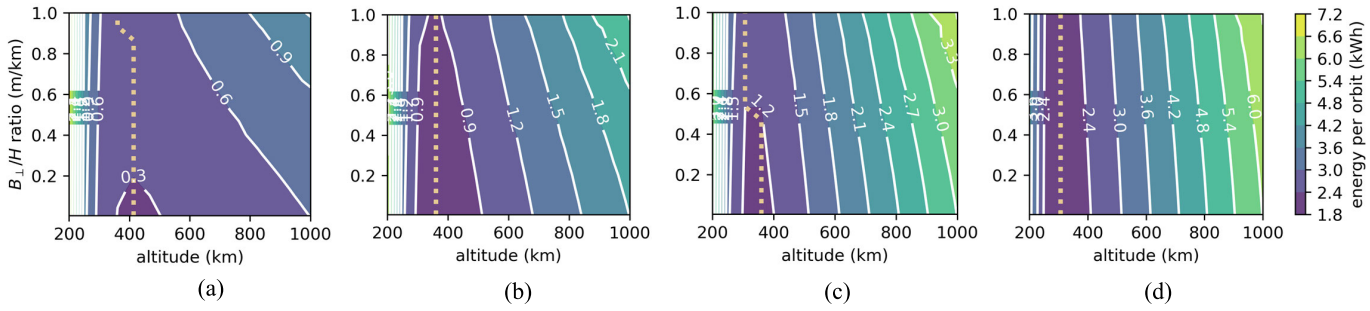

Fig. 10. Total energy demand per orbit, considering a 125-kg satellite on a helix trajectory with S/m = 0.005 m2/kg and a transmitting SAR instrument. (a) Case ζ_{orbit} = 5%. (b) Case ζ_{orbit} = 15%. (c) Case ζ_{orbit} = 25%. (d) Case ζ_{orbit} = 50%.

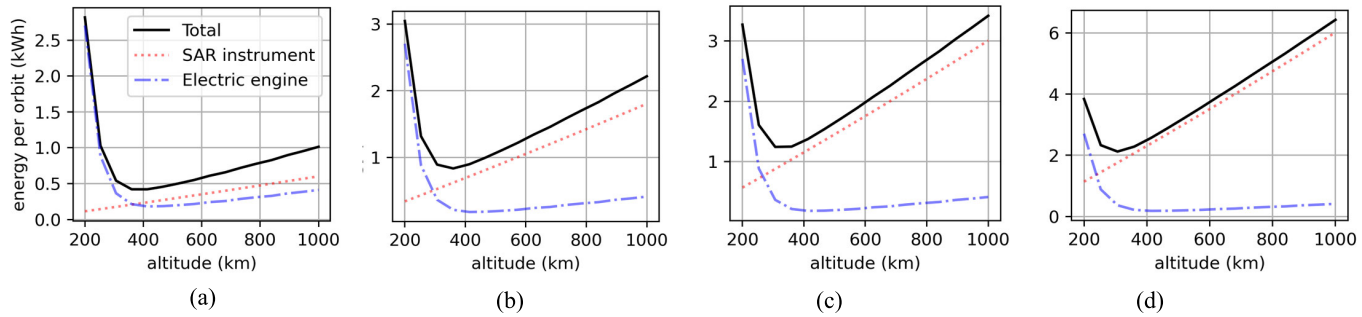

Fig. 11. Contribution to the total energy demand per orbit for the case $B\perp/H$ = 0.8 m/km, considering a 125-kg satellite on a helix trajectory with S/m = 0.005 m^2/kg and a transmitting SAR instrument. (a) Case ζ_{SAR} = 5%. (b) Case ζ_{SAR} = 15%. (c) Case ζ_{SAR} = 25%. (d) Case ζ_{SAR} = 50%.

Fig. 10 shows the resulting maps for the energy demand per orbit $E_{s/c}$ in kWh as a function of the orbit altitude and the baseline-to-altitude ratio, for the case of a 125-kg satellite with S/m = 0.005 m^2/kg on a helix relative trajectory and a transmitting SAR for the four different orbit duty cycles. In the figures, the yellow dashed line represents the condition of minimum energy demand per orbit, for each $B_\perp/H$ value. As a result, for various baseline-to-altitude ratios, we can identify the optimal orbit altitude condition, which depends on the orbit duty cycle ζ_{orbit}. As expected, a lower orbit duty cycle results in a lower contribution of the energy demand of the SAR instrument, resulting in a higher optimal altitude, with the solution driven by the energy demand of the engine. On the other hand, a higher duty cycle (i.e., ζ_{orbit} = 25% or 50%) results in a higher impact of the SAR instrument on the energy per orbit, specifically, increasing the demand at higher altitudes. Consequently, the optimal orbit altitude is lower for higher η_{SAR}. For example, we consider the case of a 400-m orthogonal baseline for an orbit altitude of 500 km (similar to the TanDEM-X case), obtaining a $B_\perp/H$ ratio of 0.8 m/km. Recall that the $B_\perp/H$ is intended as the ratio computed at the initial condition for u = 0. For a short orbit duty cycle (as in the case of 5% and 15%), the baseline can be considered quasi-constant even for a helix configuration. On the other hand, for the case of a higher orbit duty cycle, the baseline cannot be considered constant anymore, and the value of $B_\perp/H$ is used for the formation initialization. In addition, from the graphs in Fig. 10, we can identify the corresponding required energy per orbit for this condition. Specifically, we observe that the optimal orbit altitude for a $B_\perp/H$ ratio of 0.8 m/km is always lower than the selected 500 km for the TanDEM-X case, and we can compute the corresponding minimum energy, keeping the same $B_\perp/H$ and reducing the orbit altitude to the optimal one (H_{opt}). To better visualize such considerations, Fig. 11 provides the cuts of the energy per orbit for $B_\perp/H$ = 0.8 m/km. Specifically, the two contributions from the transmission of the SAR instrument and the electric engine are shown, together with the required total energy per orbit for different orbit duty cycles (as in Fig. 10). From these plots, we can clearly see how the main contribution at lower altitudes is caused by the energy required by the electric engine to keep the orbit altitude and the formation geometry. This contribution depends exclusively on the orbit altitude and the a $B_\perp/H$ ratio, while it is independent of the orbit duty cycle. On the other hand, the contribution due to the SAR instrument increases at higher altitudes and higher duty cycles, while it is independent of the $B_\perp/H$ ratio. We observe how, at higher altitudes, the contribution of the SAR instruments becomes predominant compared to the electric engine requirement for higher duty cycles, as in Fig. 11(c) and (d), causing the shift of the optimal condition toward a lower orbital altitude. Summing up these two contributions, we obtain the total energy required per orbit (see the black line in the graphs of Fig. 11). The optimal condition is identified by the minimum of the total energy per orbit: it is achieved for lower orbit altitudes as the orbit duty cycle increases, going from about 380 km at ζ_{orbit} = 5% to about 306 km for ζ_{orbit} = 50%.

The results of these considerations are reported in Table III, which shows the optimal altitude for the selected baseline-to-altitude ratio, the energy per orbit at 500 km, and the energy per orbit at the optimal altitude. We can observe an improvement from 5% to 15% of the energy per orbit,

TABLE III

COMPARISON OF THE REQUIRED ENERGY PER ORBIT AT 500 KM AND H_{opt} ALTITUDES, FOR THE CASE $B_\perp/H$ = 0.8 m/km AND S/m = 0.005 m^2/kg

Parameter	Case			
Duty Cycle ζ_{orbit} (-)	5%	15%	25%	50%
Optimal altitude from delta-v maps in Fig. 8 (km)	409			
Optimal altitude from energy maps in Fig. 12 (km)	380	360	320	306
Energy per orbit at 500 km (kWh)	0.42	1.1	1.6	3.1
Minimum energy per orbit at H_{opt} (kWh)	0.33	0.74	1.09	1.97
Improvement of energy per orbit from 500 km to H_{opt}	20%	31%	32%	38%

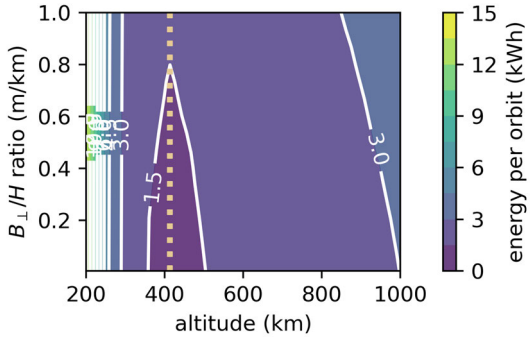

Fig. 12. Total energy per orbit, with a 125-kg satellite on a helix trajectory with S/m = 0.025 m^2/kg and a transmitting SAR.

moving the optimal orbit altitude. As expected, the larger improvement corresponds to a larger duty cycle ζ_{orbit}, and therefore, this analysis is more beneficial for a mission design where the satellite should transmit for a larger fraction of the orbit. In addition, the optimal orbit altitude to minimize the propellant consumption is reported as well: we observe that this value is about 409 km for the case under analysis and corresponds to a higher altitude compared to the results of the energy analysis. Consequently, it is important to recall that going in the direction of lower orbit altitude improves the energy demand per orbit, but, at the same time, it results in a nonoptimal solution from the formation maintenance point of view, requiring more propellant to control the formation.

Both considerations should be accounted for during the design of a mission scenario, and a tradeoff must be performed to assess the feasibility of selecting lower orbital altitudes. For example, for the scenario described in Table III, selecting the optimal altitudes from the energy analysis corresponds to an increase in the delta-velocity budget of 10% for the case of η_{SAR} of 5%, and up to 60% for the case of ζ_{orbit} of 50%. This aspect must be carefully considered during the mission design.

Similar considerations are valid for the case of S/m = 0.025 m^2/kg. For simplicity, only the case with ζ_{orbit} = 25% has been reported in Fig. 12. Comparing the value to the case in Fig. 10(c), first we observe an increase in the energy per

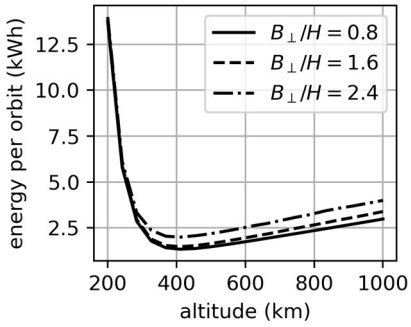

Fig. 13. Energy demand per orbit for three different values of $B_\perp/H$ ratios, considering a 125-kg satellite on a helix trajectory with S/m = 0.005 m^2/kg and a transmitting SAR instrument.

orbit at the same orbit altitudes, and at the same time an increase in the optimal altitude H_{opt} (see the yellow dashed line). As shown in Fig. 8, an increase in the optimal altitude is also present in the delta-velocity analysis. This behavior is caused by the larger area-to-mass ratio, which impacts mainly the control effort at lower orbital altitudes. The larger S/m ratio results in a higher Δv budget at lower altitudes: for the case of S/m = 0.025 m^2/kg, the altitude to obtain a minimum delta-v condition is about 518 km, in contrast to the 409 km of S/m = 0.005 m^2/kg. Similarly, the optimal altitude from the energy analysis increases from 320 to 408 km, respectively.

A similar behavior would be observed for other orbit duty cycles. This is an important result, as for the scenarios under analysis, we demonstrated that the altitude to get minimum energy demand per orbit can be below the 500-km altitude when in combination with smaller S/m ratios. This analysis can open up new applications at very LEOs, considering a mission design that combines both SAR instrument and formation control considerations. The selection of minimum energy conditions is critical to optimize the satellite's battery and solar panel design, which influences not only the wet mass at launch, but also the attitude control and the propulsion system design.

In addition, we performed a more extensive analysis to assess the impact of larger values of $B_\perp/H$. Specifically, starting from the analysis in Fig. 12, we examined the impact of doubling or tripling the baseline on the minimum energy curve. By keeping a constant altitude, this procedure allows us to consider the effect of larger baselines on the system performance. Larger baselines can be associated with longer wavelengths: for example, a factor of three starting from Ka-band is representative of SAR operations in X-band. The results are reported in Fig. 13, which depicts the conditions of $B_\perp/H$ equal to $[0.8, 1.6, 2.4]$ m/km for an orbit duty cycle of 15%. As the baseline increases, to keep similar performance at longer wavelengths, the power demand per orbit is higher and, therefore, it is even more important to reduce the orbit altitude.

Such consideration makes the proposed analysis even more relevant for frequency bands lower than the considered Ka-band, where larger baselines are required to achieve the same height of ambiguity.

TABLE IV
SYSTEM PARAMETERS FOR THE DESIGN EXAMPLE 1

Parameters	Value
Central Frequency (GHz)	35.5
Bandwidth (MHz)	100
Number of looks	52
Coherence	0.8
Satellites S/m ratio (m^2/kg)	0.005
Deputy 1 $B_\perp/H$ ratio at $u = 0$ (m/km)	0.4
Deputy 2 $B_\perp/H$ ratio at $u = 0$ (m/km)	0.1
Orbit duty cycle ζ_{orbit}	15%

IV. RESULTS AND DISCUSSION

This section presents some design examples for the methodology described in Section III, which provides a criterion for identifying the optimal orbit altitude to minimize the energy requirement and delta-velocity budget for a multistatic SAR system. Each map in Section III can be obtained for different mission configurations. Specifically, we investigate the feasibility of different formation configurations, including the possibility of fixed-baseline, by analyzing two different scenarios.

1) *Design Example 1:* Multistatic SAR system with three satellites in a nested helix configuration.
2) *Design Example 2:* Same as in Example 1, with an additional analysis to estimate the impact of a fixed-baseline configuration, in combination with helix one.

The concept of fixed baseline has already been studied in the literature [26] and shows potential improvements in SAR performance. Specifically, it removes the baseline variation in time of the helix configuration, as in TanDEM-X. The concept of maintaining the baseline constant during the satellite motion is enhanced by the possibility of implementing a continuous thrust with electric engines to compensate for the natural oscillation in the across-track direction of the relative motion. A similar concept for passive L-band interferometry was proposed in [50], where a triangular formation of three satellites was exploited to increase the virtual aperture of a passive interferometer. In this work, we address the possibility of including short-time, fixed-baseline operation in combination with the baseline helix operation to assess the impact on the delta-velocity budget and the optimal altitude selection.

A. Design Example I (Three Satellites in Helix Configuration)

The first design example considers a multistatic SAR system with three satellites in a nested helix configuration. Some studies in this direction were conducted in [18] and [51] to evaluate the performance of multiple baselines in a single-pass configuration. The parameters of the design example are shown in Table IV. The system operates in Ka-band, with three identical platforms: one primary satellite and two secondary ones. The two secondary satellites are characterized by baseline-to-altitude ratios of 0.4 and 0.1 m/km, respectively, starting from the outcomes of [51]. The geometry of this first design example is shown in Fig. 14. The helicoidal behavior

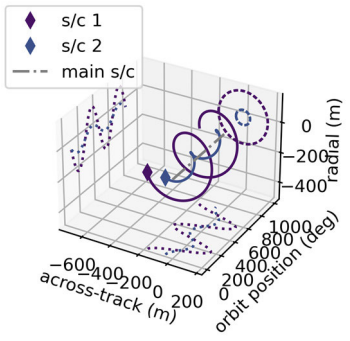

Fig. 14. Design example 1: multibaseline three satellite formation in nested helix configuration.

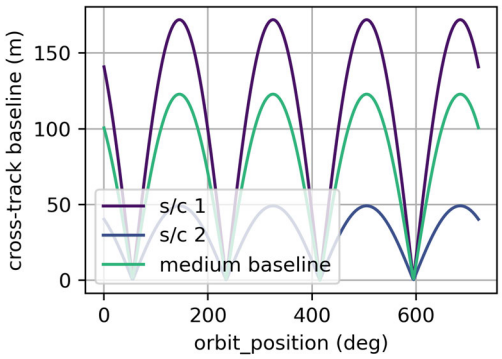

Fig. 15. Design example 1: time evolution of the perpendicular baselines.

is represented around the primary satellite as a function of orbit position in time, for two orbital periods. The nested helix configuration is shown for the value of the perpendicular baseline at 460 km of altitude: 172 and 43 m, respectively. The graph also represents the projection in the radial and across-track direction. This configuration is similar to the one described in [51], where the benefit of a third satellite in the helix configuration was analyzed to improve the final interferogram. Specifically, this geometry generates two main baselines between the secondaries and the primary satellite, and one additional baseline between the two secondaries. The time evolution of these three perpendicular baselines is shown in Fig. 15, where the latter is denoted as the medium baseline. We can observe that the perpendicular baseline generated by a helix configuration varies in time due to the nature of the relative dynamics. Using the maps in Figs. 8 and 10, we obtain the optimal altitude that minimizes the delta-v budget and the energy consumption for the secondary satellite. Note that we are considering the performance of the two secondaries with respect to the primary satellite.

The achieved DEM has a height accuracy (90th percentile) of 35 cm, considering 52 looks and a coherence level of 0.8, as shown in Fig. 5. The corresponding optimal altitude for the first deputy of 360 km minimizes the energy demand to 765 Wh. On the other hand, the delta-v is minimized for an orbit altitude of 465 km, with a daily delta-v of 0.4 m/s. Reducing the orbit altitude to 360 km from the energy analysis causes an increase in the delta-v of a factor of 1.5.

The corresponding optimal altitude and energy demand of the second deputy are similar to the values obtained for the primary spacecraft: 360 km and 750 Wh, respectively. As for the previous case, the optimal altitude that minimizes the delta-v is higher, corresponding to 519 km. For this second case, reducing the optimal orbit altitude to 360 km causes an increase in the delta-v of a factor of 2.

This result demonstrated that, for both secondary satellites, we obtain the same optimal orbit altitude, i.e., 360 km, which minimizes the energy consumption, but a different orbit altitude that minimizes the delta-v budget, requiring a proper tradeoff of the final geometry selection. Specifically, depending on the specific scenario, the minimization of the delta-v might be more significant than the minimization of the energy demand, or vice versa. The maps in Figs. 8 and 10 provide a preliminary guideline for the initial stage of the mission design, suggesting that an investigation of orbit altitude below 500 km might be beneficial for the tradeoff analysis. However, from an operational point of view, maintaining an orbit altitude below 500 km brings the challenge of more frequent maneuvers to compensate for the atmospheric drag. Such aspects must be considered during the design of the mission. As explained in Section I, keeping the baseline fixed can improve the current performance of the XTI-SAR. For this reason, Section IV-B focuses on the possibility of introducing a fixed-baseline configuration during mission operations.

B. Design Example 2 (Impact of Fixed-Baseline Configuration)

The second design example considers the same parameters as Table IV and evaluates the impact on the mission design of a fixed-baseline configuration. As demonstrated in [26], the delta-velocity budget to keep a constant baseline increases proportionally with the spacecraft separation. The analysis in [26] shows how a feasible delta-velocity budget can be obtained from the mission design point of view with baseline-to-altitude ratios below 0.2 m/km. For this reason, this section analyses two possible scenarios: keeping the same $B_\perp/H$ ratios of Table IV, and scaling down the ratio to get $B_\perp/H < 0.2$ m/km.

First, using the same procedure of Section IV-B, we compute the maps for the fixed-baseline configuration. Figs. 16 and 17 provide the delta-velocity budgets and the total energy demand, considering the maintenance of parallel tracks. Comparing the results with Section IV-B, we observe that the daily delta velocity budget increases to a maximum of 120 m/s/day for high altitude and large $B_\perp/H$, as expected. In addition, we identify a significant increase in the energy demand, up to 18 kWh. Only considering a $B_\perp/H < 0.2$ m/km, provides lower delta-velocity and energy budgets. Considering the initial conditions of Table IV, we imposed a forced dynamical evolution to keep parallel relative tracks. Specifically, the relative orbital position across the track is kept constant in time, thanks to a continuous thrust, as in [26]. The secondary satellites 1 and 2 produce a large and a small orthogonal baseline with the primary satellite, and a combined medium baseline between them. This allows the generation of multibaseline interferograms for the accurate DEM [51]. To analyze the effect of including a short fixed-baseline phase

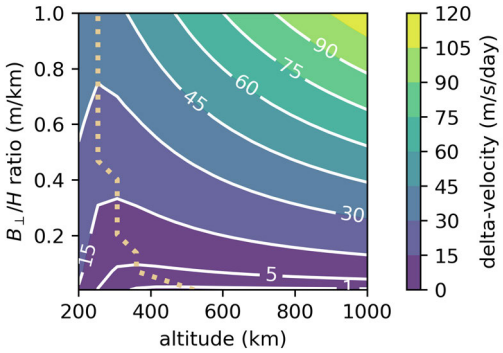

Fig. 16. Control effort in terms of daily velocity variation Δv for absolute and relative orbit maintenance. Fixed-baseline relative trajectory with $S/m = 0.005$ m^2/kg.

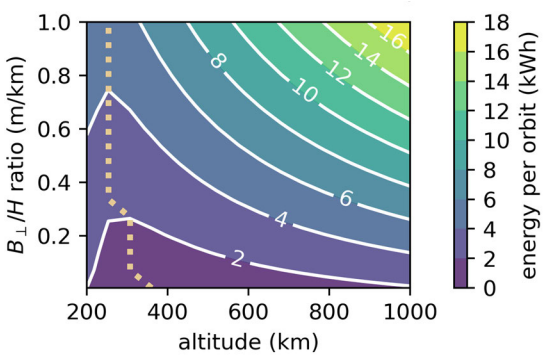

Fig. 17. Total energy per orbit, considering a 125-kg satellite on a fixed-baseline trajectory with $S/m = 0.005$ m^2/kg and a transmitting SAR instrument.

for a space mission in combination with helix configuration, we compare the daily delta-v and the energy demand per orbit, considering one day of SAR image acquisition, with one primary satellite and two secondaries. We also assume all the satellites to have the same mass and SAR instrument on board. The mission is initialized with a baseline-to-altitude ratio of 0.4 and 0.1 m/km for each secondary. We analyze the spacecraft budgets under the following scenarios.

1) Nested helix relative trajectories (see Fig. 14).
2) Fixed-baseline acquisition under parallel relative tracks.

Table V shows the results for the baseline-to-altitude ratio of 0.4 and 0.1 m/km. For case 1), under nested helix relative trajectories, the results are the same as the design example I, and were already discussed in Section IV-A. Considering a fixed-baseline configuration for case 2) for a short time causes a change in the mean budgets in terms of delta velocity and energy demand. Specifically, we assumed the same baseline-to-altitude ratio as for the helix case. As shown in Fig. 17, each value of $B_\perp/H$ corresponds to an optimal altitude, different from the optimal condition of the helix configuration. The results are shown in Table V. First, we distinguished between the optimal altitude condition from the delta-v analysis and the one related to the energy per orbit. For scenarios 1) and 2), the optimal altitude for minimizing the energy consumption is lower than the optimal altitude for minimizing the delta-v. In addition, we can observe how the optimal altitude for the

TABLE V
VELOCITY AND ENERGY BUDGET FOR DESIGN EXAMPLE 2

Deputy	**s/c 1**		**s/c 2**	
Case	**a) helix**	**b) fixed**	**a) helix**	**b) fixed**
$B_\perp/H$ (m/km)	0.4	0.4	0.1	0.1
Optimal altitude for minimum energy consumption				
H_{opt} (km)	360	260	360	300
min $E_{s/c}$ (kWh)	0.75	2.52	0.70	1.31
Optimal altitude for minimum delta-v				
H_{opt} (km)	465	304	520	360
min Δv (m/s/day)	0.45	18.5	0.12	5.1
Trade-off selected altitude				
$H_{selected}$ (km)	400			
Δv (m/s/day)	0.5	20.4	0.3	5.5
$E_{s/c}$ (kWh)	0.81	3.30	0.78	1.58

fixed-baseline acquisition is always lower than the suggested one for the helix case.

Furthermore, considering a mission design with a more extended acquisition phase in a nested helix configuration (case 1), we consider the possibility of adding a short phase with fixed-baseline acquisition, considering the following rationale. First, multiple days are scheduled with a nested helix configuration. As the baseline varies in time, the accuracy of the acquisition is affected by such behavior. Then, the formation is reconfigured in the fixed-baseline configuration, and interferometric acquisitions are performed for multiple orbital revolutions to improve the accuracy for selected regions of the Earth's surface. Considering a mission scenario where the main formation configuration is based on nested helices, the higher delta-v and energy budgets for the short fixed-baseline configuration should be considered during the mission design. Concerning the delta-velocity budget, the impact on the mission design should be minimized, reducing the frequency of the fixed-baseline phases. To assess the feasibility of such an approach, a tradeoff analysis is performed to select a suboptimal orbit altitude that accommodates both the requirements of the two different formation configurations and the minimum velocity and energy budgets. The results of this analysis are reported in Table V, selecting a suboptimal altitude of 400 km for the three-satellite system. For example, we consider the values in Table V for the tradeoff altitude. Considering a frequency of observation under a fixed-baseline configuration for one day per month, the system design should consider the following increase on the monthly delta-v budget.

1) For deputy 1, the monthly delta-v increases from 15 to 35 m/s, corresponding to an increase of a factor of 2.
2) For deputy 2, the monthly delta-v increases from 9 to 14 m/s, corresponding to an increase of a factor of 1.5.

Similarly, the energy demand per orbit during configuration 2) increases by a factor of 4 and 2 compared to the energy demand for phase 1), for deputy 1 and 2, respectively. During the design of the mission, it is essential to assess if the onboard batteries can cover this increase in energy demand, or if larger batteries or solar panels must be considered within the system design.

TABLE VI
VELOCITY AND ENERGY BUDGET FOR SMALL BASELINE-TO-ALTITUDE RATIOS

Case	**helix**	**fixed**	**helix**	**fixed**
$B_\perp/H$ (m/km)	0.05	0.05	0.02	0.02
Optimal altitude for minimum energy consumption				
H_{opt} (km)	360	320	360	346
min $E_{s/c}$ (kWh)	0.78	0.95	0.73	0.80
Optimal altitude for minimum delta-v				
H_{opt} (km)	690	410	780	480
min Δv (m/s/day)	0.06	2.8	0.05	1.2

An additional consideration must be made on the tradeoff altitude in Table V. The tradeoff altitude was selected to minimize the worsening of both energy demand and delta-v budget, with a priority given to Δv due to its direct impact on propellant mass and mission duration. In contrast, increased energy demand can be more flexibly managed through temporary enhancements in power availability (e.g., solar panels and batteries) during specific operational windows. As a result, the tradeoff altitude is selected so that the increase in delta-v for the fixed-baseline configuration [case (b)] is limited to 10%, while the worsening in the energy demand is limited to 30%. These thresholds reflect a balanced compromise and can be adapted depending on the mission architecture and subsystem constraints. From Table V, we can observe how for satellite 1, the energy demand increases of about 20%–30% for both cases a) and b) at an altitude of 400 km. Similarly, for satellite 2, the increase is about 10%–20%. For this case, the impact of a short phase in a fixed-baseline configuration is lower than for the cases with larger $B_\perp/H$. We can also observe that the suboptimal orbit altitude, resulting from the tradeoff selection, is between the optimal conditions of helix and fixed-baseline. This difference may be considered in a future design study to optimize the mission design further. Furthermore, the suboptimal altitude is lower than the typical orbital altitudes for SAR missions (around 500 km), especially when the fixed-baseline acquisition phase is introduced, suggesting that a lower orbit altitude could be investigated depending on the application and the mission scenario.

This aspect appears particularly attractive for small $B_\perp/H$ ratios (<0.1), as such a condition guarantees a similar requirement from the energy point of view, as shown in Table VI. Considering a ratio of 0.05 and 0.02, a 10% increase is observed in the energy demand per orbit, resulting in a small impact on the design of the power subsystem. For example, the subsystem margins during the design of the power systems are typically set to 30%; the 10% increase observed in Table VI could therefore be covered by the system margins. On the other hand, considering the solution for the minimum delta-v, we compute the delta-v required by the formation over one month of operation. Similar to the previous analysis, we compared the delta-v considering 30 days of helix configuration, and, as the second solution, we added a total of one day in the fixed helix

configuration. The delta-v sees an increase of a factor of 2.5 and 1.4 for the cases of 0.05 and 0.02, respectively. Note that considering such a small $B_\perp/H$ ratios result in short baselines of a few tens of meters, especially at low orbit altitude. As demonstrated in a recent ESA study, TriHex, the feasibility of a formation with short intersatellite distance in the range of 5–10 m is mainly limited by the precision of the relative navigation and control system. Submillimeter accuracy in the relative navigation was demonstrated by the PROBA-3 mission [52]; while the VISOR study demonstrated the capability of a 6U CubeSat to keep the on-board autonomous navigation error in the relative position below 1-cm level [53].

A final consideration on the corresponding propellant mass has been carried out. Specifically, without losing generality, we have considered an electric engine with a specific impulse of in the order of 2000 s, in line with the currently available hall thrust engines for small satellites. Considering the delta-v required by the helix and fixed configuration with $B_\perp/H$ in Table VI, the corresponding mass of propellant for one day of formation maintenance corresponds to about 0.4 and 8.5 g per day, for the helix and the fixed configuration, respectively. We can observe how the propellant required by the fixed configuration is higher, as expected, but its feasibility must be assessed depending on the mission selection.

V. Conclusion

A procedure to evaluate the optimal orbit altitude for a formation of two or more satellites was proposed to provide a criterion for the geometry and altitude selection of single-pass (multibaseline) SAR interferometry for DEM generation. This approach derives a model based on important parameters that can be used to assess and optimize the performance and the cost of a space mission in SAR, such as the height accuracy, the delta-velocity budget, and the energy demand per orbit cycle. Two configurations were analyzed: the multiple helix geometry, similar to TanDEM-X, and the fixed-baseline condition. The first one provides promising results, showing how a lower altitude than the one commonly used for SAR missions can be selected to minimize energy consumption. Many current and past missions are launched at about 500-km altitude or higher. In comparison, some potential benefits could be achieved with altitudes around 400 km, when including the power demand of the SAR instrument and the control effort to keep the absolute orbit and the relative trajectory, especially as the orbit duty cycle increases.

For formations with a fixed baseline, a higher control effort is generally required due to the nature of the continuous thrust to compensate for the natural oscillations of the relative motion. However, for short baselines, we demonstrated that a mission based on helix geometry could include an operational phase, up to a few days per month, with fixed-baseline maintenance without impacting the spacecraft design and configuration. For a short $B_\perp/H$ ratio (e.g., 0.05 and 0.02 m/km), the energy demand per orbit (Wh) increases by less than 10% for the fixed-baseline phase. In addition, a fixed-baseline configuration can improve the SAR interferometric performance compared to the time-variable helix baseline, especially for high-frequency bands (e.g., Ka-band), where shorter baselines are required to achieve a given height of ambiguity. The model proposed in this work can also be exploited for different formation configurations for fixed-baseline realization or CubeSat-size platforms with SAR instruments. This work, therefore, makes a relevant contribution to future single-pass spaceborne interferometric missions based on formations of satellites for high-quality DEM generation.

Acknowledgment

The authors sincerely acknowledge their colleagues Prof. Gerhard Krieger and Dr. Markus Bachmann for the productive and in-depth discussions. For retrieving statistics on current and past space missions, information from ESA Database and Information System Characterizing Objects in Space (DISCOS) has been used. ESA DISCOS is a single-source reference for launch information, object registration details, launch vehicle descriptions, as well as spacecraft information for all trackable, unclassified objects. They acknowledge ESA's efforts to maintain and operate this database with its APIs.

References

[1] A. Moreira, P. Prats-Iraola, M. Younis, G. Krieger, I. Hajnsek, and K. P. Papathanassiou, "A tutorial on synthetic aperture radar," *IEEE Geosci. Remote Sens. Mag.*, vol. 1, no. 1, pp. 6–43, Mar. 2013, doi: 10.1109/MGRS.2013.2248301.

[2] R. Bamler and P. Hartl, "Synthetic aperture radar interferometry," *Inverse Problems*, vol. 14, no. 4, pp. R1–R54, Aug. 1998, doi: 10.1088/0266-5611/14/4/001.

[3] P. A. Rosen et al., "Synthetic aperture radar interferometry," *Proc. IEEE*, vol. 88, no. 3, pp. 333–382, Mar. 2000.

[4] R. F. Hanssen, *Radar Interferometry: Data Interpretation and Error Analysis*. Dordrecht, The Netherlands: Springer, 2001.

[5] F. Gini and F. Lombardini, "Multibaseline cross-track SAR interferometry: A signal processing perspective," *IEEE Aerosp. Electron. Syst. Mag.*, vol. 20, no. 8, pp. 71–93, Aug. 2005, doi: 10.1109/MAES.2005.1499278.

[6] G. Franceschetti, A. Iodice, M. Migliaccio, and D. Riccio, "A novel across-track SAR interferometry simulator," *IEEE Trans. Geosci. Remote Sens.*, vol. 36, no. 3, pp. 950–962, May 1998, doi: 10.1109/36.673686.

[7] S. N. Madsen, H. A. Zebker, and J. Martin, "Topographic mapping using radar interferometry: Processing techniques," *IEEE Trans. Geosci. Remote Sens.*, vol. 31, no. 1, pp. 246–256, Jan. 1993, doi: 10.1109/36.210464.

[8] H. A. Zebker and J. Villasenor, "Decorrelation in interferometric radar echoes," *IEEE Trans. Geosci. Remote Sens.*, vol. 30, no. 5, pp. 950–959, Sep. 1992, doi: 10.1109/36.175330.

[9] S. N. Madsen, J. M. Martin, and H. A. Zebker, "Analysis and evaluation of the NASA/JPL TOPSAR across-track interferometric SAR system," *IEEE Trans. Geosci. Remote Sens.*, vol. 33, no. 2, pp. 383–391, Mar. 1995, doi: 10.1109/TGRS.1995.8746019.

[10] F. K. Li and R. M. Goldstein, "Studies of multibaseline spaceborne interferometric synthetic aperture radars," *IEEE Trans. Geosci. Remote Sens.*, vol. 28, no. 1, pp. 88–97, Jan. 1990, doi: 10.1109/36.45749.

[11] J. J. van Zyl, "The shuttle radar topography mission (SRTM): A breakthrough in remote sensing of topography," *Acta Astronautica*, vol. 48, nos. 5–12, pp. 559–565, Mar. 2001, doi: 10.1016/s0094-5765(01)00020-0.

[12] A. Moreira et al., "TanDEM-X: A TerraSAR-X add-on satellite for single-pass SAR interferometry," in *Proc. IEEE Int. Geosci. Remote Sens. Symp.*, Sep. 2004, pp. 1000–1003, doi: 10.1109/IGARSS.2004.1368578.

[13] G. Krieger et al., "TanDEM-X: A satellite formation for high-resolution SAR interferometry," *IEEE Trans. Geosci. Remote Sens.*, vol. 45, no. 11, pp. 3317–3341, Nov. 2007, doi: 10.1109/TGRS.2007.900693.

[14] M. Zink et al., "TanDEM-X: 10 years of formation flying bistatic SAR interferometry," *IEEE J. Sel. Topics Appl. Earth Observ. Remote Sens.*, vol. 14, pp. 3546–3565, 2021, doi: 10.1109/JSTARS.2021.3062286.

[15] S. Huber, M. Younis, and G. Krieger, "The TanDEM-X mission: Overview and interferometric performance," *Int. J. Microw. Wireless Technol.*, vol. 2, nos. 3–4, pp. 379–389, Aug. 2010, doi: 10.1017/s1759078710000437.

[16] M. Bachmann et al., "The TanDEM-X mission phases—Ten years of bistatic acquisition and formation planning," *IEEE J. Sel. Topics Appl. Earth Observ. Remote Sens.*, vol. 14, pp. 3504–3518, 2021, doi: 10.1109/JSTARS.2021.3065446.

[17] S. Leinss and P. Bernhard, "TanDEM-X: Deriving InSAR height changes and velocity dynamics of great aletsch glacier," *IEEE J. Sel. Topics Appl. Earth Observ. Remote Sens.*, vol. 14, pp. 4798–4815, 2021, doi: 10.1109/JSTARS.2021.3078084.

[18] J. Mittermayer et al., "MirrorSAR: An HRWS add-on for single-pass multi-baseline SAR interferometry," *IEEE Trans. Geosci. Remote Sens.*, vol. 60, 2022, Art. no. 5224018, doi: 10.1109/TGRS.2021.3132384.

[19] K. Thangavel et al., "A distributed satellite system for multibaseline AT-InSAR: Constellation of formations for maritime domain awareness using autonomous orbit control," *Aerospace*, vol. 10, no. 2, p. 176, Feb. 2023, doi: 10.3390/aerospace10020176.

[20] M. Grasso, A. Renga, G. Fasano, M. D. Graziano, M. Grassi, and A. Moccia, "Design of an end-to-end demonstration mission of a formation-flying synthetic aperture radar (FF-SAR) based on microsatellites," *Adv. Space Res.*, vol. 67, no. 11, pp. 3909–3923, Jun. 2021, doi: 10.1016/j.asr.2020.05.051.

[21] M. Lavalle et al., "Distributed aperture radar tomographic sensors (DARTS) to map surface topography and vegetation structure," in *Proc. IEEE Int. Geosci. Remote Sens. Symp. (IGARSS)*, Jul. 2021, pp. 1090–1093, doi: 10.1109/IGARSS47720.2021.9553170.

[22] S. Tebaldini, M. Manzoni, L. Ferro-Famil, F. Banda, and D. Giudici, "FDM MIMO spaceborne SAR tomography by minimum redundancy wavenumber illumination," *IEEE Trans. Geosci. Remote Sens.*, vol. 62, 2024, Art. no. 5207119, doi: 10.1109/TGRS.2024.3371267.

[23] S. D'Amico and O. Montenbruck, "Proximity operations of formation-flying spacecraft using an eccentricity/inclination vector separation," *J. Guid., Control, Dyn.*, vol. 29, no. 3, pp. 554–563, May 2006, doi: 10.2514/1.15114.

[24] E. R. S. Filho, M. Rodriguez-Cassola, R. Katz, J. Matar, and A. Moreira, "Fuel-efficient formation strategies for cross-track multi-static SAR constellations," in *Proc. IEEE Int. Geosci. Remote Sens. Symp.*, Pasadena, CA, USA, Jul. 2023, pp. 4556–4559, doi: 10.1109/IGARSS52108.2023.10282868.

[25] E. Rodriguez and J. M. Martin, "Theory and design of interferometric synthetic aperture radars," *IEE Proc. F Radar Signal Process.*, vol. 139, no. 2, pp. 147–159, 1992, doi: 10.1049/ip-f-2.1992.0018.

[26] F. Scala, G. Krieger, and M. Villano, "Investigation of fixed across-track baselines for distributed spaceborne SAR systems," in *Proc. EUSAR*, Munich, Germany, Apr. 2024, pp. 32–37.

[27] F. Scala, G. Krieger, and M. Villano, "Investigation of multiple-satellite formation configurations for single-pass synthetic aperture radar interferometry," in *Proc. IAF Earth Observ. Symp.*, Milan, Italy, Oct. 2024, pp. 642–647.

[28] N. H. Crisp et al., "The benefits of very low Earth orbit for Earth observation missions," *Prog. Aerosp. Sci.*, vol. 117, Aug.2020, Art. no. 100619, doi: 10.1016/j.paerosci.2020.100619.

[29] *ESA Space Debris Mitigation Requirements*, document ESA-TECQI-HO-2024-002968, Space Debris Mitigation Team, Oct. 2024, pp. 1–119. [Online]. Available: https://indico.esa.int/event/541/attachments/6306/10969/ESA-TECQI-HO-2024-002968%20-%20ESA's%20Space%20Debris%20Mitigation%20Requirments%20-%20training.pdf

[30] C. Araguz et al., "Optimized model-based design space exploration of distributed multi-orbit multi-platform Earth observation spacecraft architectures," in *Proc. IEEE Aerosp. Conf.*, Big Sky, MT, USA, Mar. 2018, pp. 1–16, doi: 10.1109/AERO.2018.8396712.

[31] S. W. Paek, S. Balasubramanian, S. Kim, and O. de Weck, "Small-satellite synthetic aperture radar for continuous global biospheric monitoring: A review," *Remote Sens.*, vol. 12, no. 16, p. 2546, Aug. 2020, doi: 10.3390/rs12162546.

[32] D. Lev, R. M. Myers, K. M. Lemmer, J. Kolbeck, H. Koizumi, and K. Polzin, "The technological and commercial expansion of electric propulsion," *Acta Astronautica*, vol. 159, pp. 213–227, Jun. 2019, doi: 10.1016/j.actaastro.2019.03.058.

[33] G. Krieger and A. Moreira, "Spaceborne bi- and multistatic SAR: Potential and challenges," *IEE Proc. Radar, Sonar Navigat.*, vol. 153, no. 3, pp. 184–198, Jun. 2006, doi: 10.1049/ip-rsn:20045111.

[34] R. Grandin, E. Klein, M. Métois, and C. Vigny, "Three-dimensional displacement field of the 2015 Mw8.3 Illapel earthquake (Chile) from across- and along-track Sentinel-1 TOPS interferometry," *Geophys. Res. Lett.*, vol. 43, no. 6, pp. 2552–2561, Mar. 2016, doi: 10.1002/2016gl067954.

[35] M. Lachaise, T. Fritz, and R. Bamler, "The dual-baseline phase unwrapping correction framework for the TanDEM-X mission—Part 1: Theoretical description and algorithms," *IEEE Trans. Geosci. Remote Sens.*, vol. 56, no. 2, pp. 780–798, Feb. 2018, doi: 10.1109/TGRS.2017.2754923.

[36] F. Lombardini and P. Lombardo, "Maximum likelihood array SAR interferometry," in *Proc. IEEE Digital Signal Process. Workshop*, Jun. 1996, pp. 358–361, doi: 10.1109/DSPWS.1996.555535.

[37] G. Krieger, A. Moreira, I. Hajnsek, M. Werner, H. Fiedler, and E. Settelmeyer, "The TanDEM-X mission proposal," in *Proc. ISPRS Workshop High-Resolution Earth Imag. Geospatial Inf. ISPRS Workshop High-Resolution Earth Imaging Geospatial Inf.*, Hannover, Germany, 2005, pp. 1–6. [Online]. Available: https://elib.dlr.de/20722/

[38] W. D. Pesnell and K. H. Schatten, "An early prediction of the amplitude of solar cycle 25," *Sol. Phys.*, vol. 293, no. 7, p. 112, Jul. 2018, doi: 10.1007/s11207-018-1330-5.

[39] J. M. Picone, A. E. Hedin, D. P. Drob, and A. C. Aikin, "NRLMSISE-00 empirical model of the atmosphere: Statistical comparisons and scientific issues," *J. Geophys. Res., Space Phys.*, vol. 107, no. A12, pp. SIA 15-1–SIA 15-16, Dec. 2002, doi: 10.1029/2002ja009430.

[40] ESA Space Debris Office, DISCOSweb. (2024). *ESA DISCOS (Database and Information System Characterising Objects in Space)*. Accessed: May 27, 2025. [Online]. Available: https://discosweb.esoc.esa.int/

[41] G. D. Krebs. (Dec. 4, 2024). *USA 276 (NROL 76) Gunter's Space Page*. [Online]. Available: https://space.skyrocket.de/doc_sdat/usa-276.htm

[42] G. D. Krebs. (Dec.4, 2024). *Quill (P-40), Gunter's Space Page*. [Online]. Available: https://space.skyrocket.de/doc_sdat/quill.htm

[43] F. Gatelli, A. M. Guamieri, F. Parizzi, P. Pasquali, C. Prati, and F. Rocca, "The wavenumber shift in SAR interferometry," *IEEE Trans. Geosci. Remote Sens.*, vol. 32, no. 4, pp. 855–865, Jul. 1994, doi: 10.1109/36.298013.

[44] S. Mazouffre, "Electric propulsion for satellites and spacecraft: Established technologies and novel approaches," *Plasma Sources Sci. Technol.*, vol. 25, no. 3, Jun. 2016, Art. no. 033002, doi: 10.1088/0963-0252/25/3/033002.

[45] W. H. Clohessy and R. S. Wiltshire, "Terminal guidance system for satellite rendezvous," *J. Aerosp. Sci.*, vol. 27, no. 9, pp. 653–658, Sep. 1960, doi: 10.2514/8.8704.

[46] A. W. Koenig, T. Guffanti, and S. D'Amico, "New state transition matrices for spacecraft relative motion in perturbed orbits," *J. Guid., Control, Dyn.*, vol. 40, no. 7, pp. 1749–1768, Jul. 2017, doi: 10.2514/1.g002409.

[47] G. Di Mauro, R. Bevilacqua, D. Spiller, J. Sullivan, and S. D'Amico, "Continuous maneuvers for spacecraft formation flying reconfiguration using relative orbit elements," *Acta Astronautica*, vol. 153, pp. 311–326, Dec. 2018, doi: 10.1016/j.actaastro.2018.01.043.

[48] Y. Ulybyshev, "Long-term formation keeping of satellite constellation using linear-quadratic controller," *J. Guid., Control, Dyn.*, vol. 21, no. 1, pp. 109–115, Jan. 1998, doi: 10.2514/2.4204.

[49] R. Bevilacqua, T. Lehmann, and M. Romano, "Development and experimentation of LQR/APF guidance and control for autonomous proximity maneuvers of multiple spacecraft," *Acta Astronautica*, vol. 68, nos. 7–8, pp. 1260–1275, Apr. 2011, doi: 10.1016/j.actaastro.2010.08.012.

[50] M. Martin-Neira, M. Piera, F. Scala, C. Colombo, A. Zurita, and B. Duesmann, "Formation flying L-band aperture synthesis mission concept," in *Proc. IEEE Int. Geosci. Remote Sens. Symp.*, Jul. 2022, pp. 7325–7328, doi: 10.1109/IGARSS46834.2022.9884089.

[51] M. Nogueira Peixoto, G. Krieger, A. Moreira, C. Waldschmidt, and M. Villano, "On the exploitation of CubeSats for highly accurate and robust single-pass SAR interferometry," *IEEE Trans. Geosci. Remote Sens.*, vol. 61, 2023, Art. no. 5217216, doi: 10.1109/TGRS.2023.3316895.

[52] J. S. Llorente et al., "PROBA-3: Precise formation flying demonstration mission," *Acta Astronautica*, vol. 82, no. 1, pp. 38–46, Jan. 2013, doi: 10.1016/j.actaastro.2012.05.029.

[53] A. W. Koenig, S. D'Amico, and E. G. Lightsey, "Formation flying orbit and control concept for virtual super optics reconfigurable swarm mission," *J. Guid., Control, Dyn.*, vol. 46, no. 9, pp. 1657–1670, Sep. 2023, doi: 10.2514/1.g007334.

Francesca Scala received the B.Sc., M.Sc., and Ph.D. (Hons.) degrees in space engineering from the Politecnico di Milano, Milan, Italy, in 2016, 2018, and 2023, respectively.

In 2022, she was a Visiting Researcher for six months at European Space Agency (ESA), Noordwijk, The Netherlands, as part of the Ph.D. research, where she developed guidance and control strategies for formation flying missions for passive L-band interferometry mission concepts. From 2023 to 2025, she was a Post-Doctoral Researcher with German Aerospace Center, Microwave and Radar Institute, Weßling, Germany, where she developed mission analysis and guidance and control algorithms for synthetic aperture radar mission concepts with multiple satellites flying in formation. Since 2025, she has been with Starion Group, Noordwijk, as a Mission Analysis Engineer for ESA, within the Earth Observation Program Department. In this role, she has been providing expertise and developing algorithms in support of ESA's ongoing Earth Observation missions, contributing across all phases from initial development through in-orbit operations. She has authored or co-authored nearly 40 papers, including peer-reviewed journal articles and proceedings of international conferences.

Dr. Scala was a recipient of European Commission LPS Student Grant by EU-ESA Copernicus Program for participation in the 2022 ESA Living Planet Symposium. She was a recipient of the ESA-ISEB IAC2021 Sponsorship for participation at the International Astronautical Congress 2022 (IAC22) and the ISEB Program in Paris, France. In addition, she has won the Best Interactive Presentation Award at the IAC22, Paris, in the "applications and operations" category.

Michelangelo Villano (Senior Member, IEEE) received the B.Sc. and M.Sc. degrees (Hons.) in telecommunication engineering from the Sapienza University of Rome, Rome, Italy, in 2006 and 2008, respectively, and the Ph.D. degree (Hons.) in electrical engineering and information technology from Karlsruhe Institute of Technology, Karlsruhe, Germany, in 2016.

From 2008 to 2009, he was a Young Graduate Trainee with European Space Research and Technology Center, European Space Agency, Noordwijk, The Netherlands, where he developed processing algorithms for ice sounding radar. Since 2009, he has been with German Aerospace Center (DLR), Microwaves and Radar Institute, Weßling, Germany, where he developed the staggered synthetic aperture radar (SAR) acquisition mode. Since 2019, he has been the Head of the NewSpace SAR Research Group, where he leads the development of cost-effective and multistatic SAR concepts for Earth monitoring. In 2017, he was a Visiting Research Scientist with the Communications, Tracking, and Radar Division, NASA Jet Propulsion Laboratory, Pasadena, CA, USA, where he adapted the staggered SAR mode to the NASA-ISRO SAR (NISAR) mission. Since 2019, he has also been a Lecturer with Ulm University, Ulm, Germany. He has authored or co-authored nearly 50 peer-reviewed journal articles, a book chapter, and over 100 papers in international conference proceedings. He holds 14 patents in the field of SAR.

Dr. Villano was a recipient of the First Place Student Paper Award at European Conference on Synthetic Aperture Radar (EUSAR) 2014, the Institute of Electrical and Electronics Engineers (IEEE) Geoscience and Remote Sensing Society (GRSS) Letters Prize Paper Award in 2015 and 2017, the Student Paper Award at Asia–Pacific Conference on Synthetic Aperture Radar (APSAR) 2015, the DLR Science Award in 2016 and 2023, the Award as Young Scientist (now Fellow) of the Werner von Siemens Ring Foundation in 2017, the Information Technology Society (ITG) Dissertation Award in 2017, the Best Paper Award at German Microwave Conference 2019, and the First Prize Best Paper Award at the APSAR 2025. In 2022, he was awarded a Starting Grant by European Research Council (ERC). He is the Co-Chair of the Working Group on "Active Microwave: Radar and SAR" of the IEEE GRSS's Technical Committee on Instrumentation and Future Technologies. He is a Distinguished Lecturer of IEEE GRSS from 2025 to 2026. He served as the Technical Program Chair for the EUSAR 2024. He serves as an Associate Editor for IEEE TRANSACTIONS ON GEOSCIENCE AND REMOTE SENSING.